~~A Semi-Analytical Calculation of 3D Pore-Related Parameters of Insect-Proof Screens~~ Semi-Analytical Calculation of Pore-Related Parameters of Wire/Woven Screens

F.-J. Granados-Ortiz[a,b,*], A. Lopez-Martinez[b,c], J. Ortega-Casanova[a], C.-H. Lai[d]
[a]Department of Mechanical, Thermal and Fluid Engineering, University of Málaga
C/ Dr Ortiz Ramos s/n, 29071 Málaga, Spain
[b]Department of Engineering, University of Almería, Almería, Spain
[c]CIAIMBITAL Research Centre, University of Almería, Almería, Spain
[d]School of Computing and Mathematical Sciences, University of Greenwich, London, UK
*Corresponding author: fjgranados@uma.es

Abstract

Wire/woven screens have a wide range of applications, from being used as simple mechanical screening device to nanoscreen wicking with nanofluids. The vast number of applications makes important to study these screens with high accuracy, to reduce errors in characterisation and performance predictions. Previous works to date focused either on the study of these screens as a two-dimensional surface (e.g. in ventilation openings as insect-proof screens) or as three-dimensional structures under important assumptions (symmetric mesh, thickness of two times their diameter, linear evolution of the pore area along the thickness). These incomplete modellings introduce errors in applications such as the estimation of permeability of the porous media (two-dimensional porosity is identical for two meshes with the same projected area of pore but different thickness) or computational simulations of ventilation in buildings/greenhouses, where these parameters are imposed as boundary condition. The present investigation shows a method to calculate three-dimensional pore related structural properties semi-analytically for the first time and for any plain square mesh. We found that when sweeping the mesh with a plane parallel to it there are up to six different zones or stretches which can be integrated by a piece-wise approach (here named Discretisation Method). Results demonstrated high accuracy in the calculation of three-dimensional porosity and constriction factor (a parameter that is calculated by integration over the pore volume). Due to the mathematical complexity in the method, a software (Aero-Screen v1.0) is available to obtain pore-related structural parameters from diameters, separations and thickness of the screen.

Keywords: woven screen, structural properties, porous characterisation, mathematical modelling

Nomenclature

Roman Symbols

$\mathcal{D}$	Discretisation.
$\mathcal{S}$	Stretch.
A	Area.
a	Sum of the x and y-thread/wire radii.
C	Limiting point in the intersection between the cylinder and the torus.
c	Crimp.
D	Diameter of a thread/wire.
d	Distance between the position of the centre of a thread/wire and a limiting point C.
e	Thickness of the screen.
f	Friction factor.
h	Vertical separation between the centre of threads.
K	Permeability.
L	Separation between threads/wires.
l	Total length of the thread/wire.
N	Number of element.
O	Position of the centre of a thread/wire with respect to an axis.
p	Horizontal separation between the centre of threads/wires.
R	Radius of a thread/wire.
Re	Reynolds number.
s	Polar angle of the cylinder.
U	Velocity of air.
u, v	Polar angles of the torus.
V	Volume.
Y	Inertial factor.
zp	Integration limits of z at each stretch partition.
i,j	Thread/wire generalised notation.
x, y, z	Cartesian coordinates.

Abbreviations

3D	Three-dimensional.
CF	Constriction factor.
CFD	Computational Fluid Dynamics.
IPS	Insect-proof screen.
WS	Wire/woven screen.

Subscripts

$\mathcal{S}_{\mathcal{D}}$	Stretch in an arbitrary discretisation.
bt	Bottom torus.
cyl	Cylinder.
lim	Limits a distance or integration limit for the upper torus.
$lim2$	Limits a distance or integration limit for the bottom torus.
p	Magnitude related to the pore.
t	Total value of a quantity.
x, y	x or y-coordinate.
hx, hy	Diameter subscript for the x or y-thread/wire.
px, py	Separation subscript for the x or y direction.
2D	Two-dimensional quantity.
3D	Three-dimensional quantity.

Greek Symbols

Δ	Magnitude difference.
ϕ	Porosity.
ρ	Density of threads/wires.
θ	Inclination angle of the thread/wire. Also contact angle.

Superscripts

$'$	Plane coordinate position.
$linear$	Quantity calculated from a linear approximation.
x,y	Thread/wire specification (x-thread or y-thread).

1. Introduction

The use of plain square woven (wire) screen (WS) meshes is very common in industrial applications such as screening filtering of elements [1], barrier to avoid the entrance of insects [2], protective mesh for gas turbine compressors [3], control of turbulence intensity [4], static mixing [5], or noise absorption [6, 7]. Amongst these examples, the use of these meshes as insect-proof screens (IPS) in greenhouses or buildings is one of the most popular applications, due to their frequent use for passive crop protection [8] and blocking the entrance of insects in buildings [9]. In greenhouses, insects are vectors of diseases to crops, and the use of IPSs represents a barrier to restrict the entrance of insects [10], reduces the use of pesticides [11], and prevents the escape of insect pollinators [12]. However, IPSs reduce ventilation rate, being detrimental in the microclimatic conditions within the greenhouse (temperature and humidity) [13]. ~~This outlines the importance of designing IPSs that maximise ventilation and block the entrance of insects.~~

Wire screens are characterised by weft and warp threads. The warp threads determine the width of the mesh, whilst the warp threads are placed in an alternated separation along the screen, creating a woven-like structure. To characterise the geometric properties of the mesh of the screens one just needs to know the separation between threads in the x (weft) and y (warp) direction L_{px} and L_{py}, the diameters of the threads in the x and y directions D_{hx} and D_{hy}, and the thickness of the screen e (see Figure 1). These parameters can be measured to characterise an existing mesh, or input into a design process to create a new mesh. In the second scenario, not all combinations are possible, as the interlacing of threads is modelled by mathematical equations that may lead to unfeasible solutions [14]. In recent years, novel processing techniques are allowing the modelling of interlaced threads forming the woven structures by different approaches. The work in [15] consists of the 3D reconstruction of woven fabrics from pictures. The software combines relevant weave parameters, colours and cross-sectional shapes to create 3D digital images of the actual woven structure. This work was not focused on the calculation of pore-related parameters, so the information provided is very limited. In [16], Fourier series are used to fit the experimental binding waves of the threads, thanks to a cross-sectional image analysis method. Fourier series for the modelling of the threads were also used in [17]. In this investigation, the reaction to mechanical loads of the woven structure was studied analytically. The aim was to develop a discrete mass-spring model of the meso/macro mechanical behaviour of a woven structure is developed. To model the deformation, Fourier series were used, since the deformed shape of the yarns is assumed

to retain its initial periodical shape. This study was of strong potential, since most works related to the mechanical response to loads in the literature use Finite Element simulations [18, 19], due to the complex shape of interlaced threads. The models in [17] were also used in more recent works such as [20], where the beam theory is used as a novelty to model the thread interactions at their cross-over points (so that these can be considered as external loads when isolating single threads); and [21], whose work led to a micromechanical model of woven structures accounting for yarn-yarn contact based on Hertz theory and energy minimisation. This modelling under loads was also extended to the field of composite modelling [22], since composites can be created also as compact woven structures [23, 24]. We have not found previous literature on how the aerodynamic ventilation or screening ability of screens is perturbed when the mesh is subject to deformations.

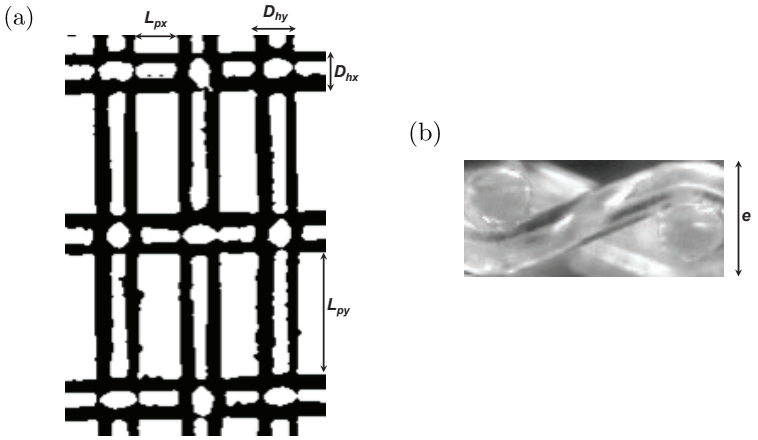

Figure 1: Microscope images of a plain square woven screen for a greenhouse (a) and its geometry through the thickness (b).

Pore-related properties have been studied in the literature, due to their importance in the mechanical performance of screen applications. For instance, in [25] the impact of pore sizes (dependent on the diameter of threads and their spacing) on the performance of superhydrophobic wire screens is studied. These screens possess interesting mechanical properties such as providing drag reduction [26] or mechanical separation of fluids having different surface tension [27]. In [25] the impact of the pore size is analysed to estimate a pore-related property, the wetted area (area of contact between water and the solid surface), and it is later used to estimate the reduction in drag. Zhao et al. [28] outlined the importance and rising popularity of metallic woven screens to enhance heat transfer [29]. Zhao et al. [28] modelled properties such as volumetric porosity, specific surface areas and conductivity for multi-layered fully symmetric screens ($D_{hx} = D_{hy} = D_h$, $L_{px} = L_{py} = L_p$, $e = 2D_h$). Their estimated parameters were approximations to reality but

sufficient to demonstrate their relevance in performance prediction. Another relevant application of woven screens is to use them as mechanical sieve. The work developed in [30] shows how screen blocking can be modelled to predict the decrease in screen performance. The grain relative size is the ratio between the average grain size (diameter) to the size of the pore. Therefore, the effective area of the pores must be calculated accurately, otherwise the modelling results can be misleading. An interesting attempt to calculate this effective area of woven screen pores is given in [31]. As the area of these "holes" is not the projected surface but a 3D deformation of it (which is larger than its projection), in this work two mathematical approaches are proposed to estimate the actual area. Following this approach, Álvarez&Oliva [32] used this accurate calculation of the 3D area of the pore hole to find a completely effective woven screen to protect crops from the entrance of an specific size insect (Chestnut Gall Wasp). The aim was to use insect-proof screens with smaller 3D hole areas than the insect thorax and abdomen size.

To obtain the pore-related properties of woven screens allows to perform CFD simulations of the ventilation of greenhouses/buildings with insect-proof screens. For instance, in [33, 34] (ventilation of greenhouses) and [9] (ventilation of a kitchen) screens are modelled as a thin porous surface on which the pore-related properties are input to model pressure drop via Darcy's law. This approach allows to simulate ventilation in large spaces without the need to simulate complex woven structure pores using CFD, which have a very small size with respect to the entire room/greenhouse. This allows to save important computational resources and reduces the complexity in the modelling as the CFD mesh is simpler. In terms of ventilation, other works in the literature [35, 36] have focused on the development of discharge coefficient models to explain the ventilation capacity of screened windows, as well as heat and mass transfer in the ventilation process. These discharge coefficients rely on the pressure drop coefficient, which requires to know beforehand the pore-related properties of the screen [37, 38, 39].

There are also applications at micro/nanoscale in which the characterisation of screens is still under research. In [40] the flow physics of wicking into micro/nano woven screens are studied experimentally, which gained relevance recently due to phase-change heat transfer and phase separation. In this work, porosity is used to calculate the volume-flow rate due to capillarity. In the calculation, a geometrical parameter (which characterises the screen sample influence) dependent on the porosity is fundamental to describe the volumetric liquid drawn into the woven screens. Similarly, [41] studied nanoscreen mesh wick and heat transfer by experimental testing in the ap-

plication of Al_2O_3 and TiO_2 nanofluids, due to their popular use in thermal applications thanks to their outstanding thermophysical properties. All the aforementioned works rely on pore-related properties to study woven screen mechanics, which evince the importance of an accurate calculation of these parameters: if their calculation is inaccurate, their study is inaccurate too, as errors are propagated in the calculation.

Finally, another important application of the characterisation of pore-related parameters in industry is to build models to characterise the aerodynamic performance of screens, which has been an important area of research for decades. Initial investigations took place many decades ago [42, 43], and continued to be studied in more recently both experimentally [44, 45, 46] and computationally [47, 48]. From this testing, and mostly experimentally, a prediction of the aerodynamic performance of the screens based on relevant parameters is achieved [39, 49]. This allows provision of industrial information in manuals (either on ventilation or filtering properties, depending on the application) for industrial screens. Thus, for a certain Reynolds number (e.g. based on the diameter of threads) and geometric characteristics (diameter of threads, spacing, thickness, porosity, constriction factor, characteristic diameters, etc.), one can classify existing screens or predict the behaviour of new designs. However, the accurate description of all screen properties is not straightforward, due to their interlaced thread shape governed by non-linear systems of equations. Despite ~~of all the work made since decades ago~~ the previous works in the literature, an exact analytical model to estimate screens aerodynamic properties does not exist.

The installation of these screens in a system creates a pressure drop which can be related to the velocity of inlet air by means of just a quadratic polynomial fit $\Delta P = \alpha U^2 + \beta U$ [12, 50, 51]. In this modelling, α and β are two coefficients related to the relevant properties of the mesh: permeability K, which is independent of the working fluid but on the geometry; and the inertial factor Y, which varies with the nature of the porous media [39, 52]. Many attempts to model the effect of flow through screens can be found in the literature, but they all show noticeable errors in the predictions. Possibly the first work in the literature addressing this topic was Eckert's memorandum for the National Advisory Committee of Aeronautics in 1942 [42], where air resistance of round wire screens with different superficial solidity (that is to say, bidimensional porosity) were studied. This line of research was continued by other researchers. It is important to point out the work by Armour and Cannon [53], who developed a model applicable for a wide range of porous media (grids, plates with holes, monofilament plastic screens, and possibly other surfaces with ordered equisized holes) as

the screen is treated as a very thin packed bed. A good model for the friction factor f was obtained for Reynolds numbers ranging between 1 and 100. The friction factor coefficient f is related to the pressure loss per unit length from the Darcy-Forchheimer equation [54]. Similar models to this one can be also found in recent works as [46, 55, 56], what evinces few improvements over the years. A significant gap as observed in the literature is that the three-dimensional approach to screens is scarce. Due to screens having a very small dimension in the direction of the thickness (z) in comparison to the warp and weft threads, it is very often to see bidimensional characterisations of the screens. For instance, it is the standard in the study of IPS in agriculture to calculate porosity as a bidimensional quantity by $\phi_{2D} = \frac{L_{px}L_{py}}{(L_{px}+D_{hy})(L_{py}+D_{hx})}$ [39, 49, 57, 58]. From these assumptions, empirical models to estimate aerodynamic properties (permeability, inertia factor, pressure drop, etc.) are constructed [39, 57]. Even from intensive work to obtain the best correlations to fit pressure drop in screen data using two-dimensional porosity estimations an unavoidable $\pm 30\%$ of dispersion in data is present [59].

The simplification of 3D structural properties to 2D structural properties of the mesh is not correct, specially due to two reasons: two screens may have the same pore size but different thickness and thus different porosities [14]; and the effective area to avoid the pass of objects or insects is not as simple as $L_{px} \times L_{py}$, but requires some 3D considerations, as studied mathematically in [31].

As mentioned above, empirical models are an aim to estimate the aerodynamic performance of screens, usually based on two-dimensional quantities. Notwithstanding, Berg [60] developed an important contribution to the field by describing permeability of porous media via characteristic features such as tortuosity (related to streamlines), characteristic length (related to the hydraulic pore), porosity (related to the fractional void volume that conducts the flow from inlet to outlet), and constriction factor (related to fluctuation in local hydraulic radii). The pore constriction/expansion or "hydrodynamic conductance" has been considered in a previous original work by Berg [61] and it represents a term to account for the variations of velocity that take place through the constriction/expansion of pores (because of conservation of mass in fluid mechanics the volume flow rate is constant) and thus reduces permeability. This term has been considered in simplified porous media in [62], and a standard deviation of the cross-sectional area of pores is also considered as a measure of the degree of constriction in [63]. Moreover, the constriction term is often grouped together with tortuosity effect [64, 65], although it has been demonstrated

in [60] that both terms must be considered separately. These relevant ideas from general porous media in [60] were imported recently to wire screens. As an attempt to find better models with less dependence on empirical modelling, Wang and coworkers developed models for the friction coefficient for different screens in [66]. These models included together for the first time the tortuosity, constriction factor and porosity in the estimation of the performance of screens. This is the only work out there on how to obtain a constriction factor of screens. However, their modelling of the constriction factor has strong limitations: it is calculated by a linear interpolation of the local variation of the area of the pore for the sake of obtaining a generalisation of the calculation, as the weave of the wire/threads of screens is a complex three-dimensional shape. Also, in their calculation they considered only symmetric meshes, thus it was not generalisable to any screen. Therefore, the calculation of the constriction factor of screens has room for improvement, since an accurate mathematical modelling of the shape of the pore does not yet exist.

To summarise the literature review discussed above, it can be concluded that wire screens porous structural properties have not been studied thoroughly. Previous works focused either on the study of these screens as a 2D surface (e.g. in ventilation openings as insect-proof screens [39, 67]: 2D porosity is identical for two meshes with the same projected area of pore but different thickness) or as 3D structures under important assumptions (symmetric mesh, rough linear approximation to the evolution of the pore area along the thickness) [66]. Other work that considered the mesh as a 3D structure have focused only on the study of the effective area of the pore to block the entrance of insects and used it to improve 2D estimated porosity values [31], porosity calculation as a void fraction not generalised to pore-related parameters [14], or have used Fourier series to characterise thread shapes under loads but not structural properties [16].

The main novelty of the present work is the proposal and application of a method (Discretisation Method) to model accurately the 3D plain square mesh pores to fill this relevant research gap in the characterisation of screens ~~aerodynamics~~. The Discretisation Method based on the different regions or stretches that the flow crosses along a mesh pore is tested and validated. This method allows to calculate accurately three-dimensional structural quantities of interest in the modelling of either symmetric and asymmetric meshes. To the knowledge of the authors, none of the previous works in the literature modelled analytically the structure of the pore to obtain structural parameters from its volume integration, being the characterisation of pore-related properties of screens very rough to date. To model (semi)analytically the mesh pores is an important contribution to

calculate quantities such as the constriction factor, which is a structural parameter of the screen only calculable by integration over the pore volume. Upon measurable (design) quantities as the diameter of the wire/threads, their spacing, and the thickness of the screen the method allows to calculate these quantities. This is implemented in the AeroScreen v1.0 software.

This investigation is useful to various applications. For instance, the semi-analytic calculation of the pore allows to input more accurate boundary conditions in the CFD simulations in ventilation of buildings/greenhouses, as screens are modelled as a thin surface (with no thickness) on which pore-related structural parameters are input to the numerical software [9, 33]. The semi-analytical modelling can be also used for the development of new designs, as one can assess the impact of changes in geometry (and in consequence on pore-related parameters) on the performance of the screen with lower errors. E.g., there are permeability or ventilation models in the literature based on pore-related parameters [35, 60] and can be used to assess permeability/ventilation when different designs are tested. In addition, the methodology in the present work has been implemented in the new AeroScreen v1.0 software, as tool for other researchers. Besides the option to input geometric data manually, this software is compatible with output files from Euclides (a software to extract screen measures from images) [67]. In consequence, pore-related structural parameters and 3D geometry reconstruction can be obtained from woven screen pictures. This gives the chance to develop mobile apps to obtain the characterisation of screens instantly by using mobile phone cameras, of interest in the supervision&maintenance of installed screens by mechanical engineers. In any case, wire/woven screens have numerous applications in industry (ventilation, mechanical screening, heat transfer&mixing in fluids, turbine protection, safety in switchgears, nanoscreen wicking with nanofluids, control of turbulence in high-speed flows, woven fabrics, etc.), thus this work is a relevant contribution to multidisciplinary knowledge in mechanical sciences.

~~A discretisation method based on the different regions or stretches that the flow crosses along a mesh pore is tested and validated. This method allows to calculate accurately three-dimensional structural quantities of interest in the modelling of either symmetric and asymmetric meshes, such as porosity or the constriction factor. This methodology outperforms the linear approximation developed in [66] for the constriction factor, and represents another way to estimate the volumetric porosity studied in [14]. Upon measurable (design) quantities as the diameter of the wire/threads, their spacing, and the thickness of the screen the method allows to calculate these quantities, which is implemented in the AeroScreen v1.0 software.~~

This manuscript is structured as follows. Section 2 describes the methods to carry out the calculation, including the modelling of the interlaced threads and the local variation of the cross-sectional area of the pores. Section 3 presents the results from the application of the method, which is applied to the calculation of the volume of the pore and constriction factor for different screens from the literature. Finally, in Section 4 the conclusions from this work are drawn. Additionally, Appendix A provides some mathematical details on the intersection between a plane and a toroid and cylinder; and Appendix B provides mathematical details on the application of the approach via stretches for the calculation of the volume integral of the pore with separation of integrals.

2. Methods

In order to develop the mathematical study, first the geometry of the interlacing of threads must be comprehended. After this, the full 3D characteristics of the pores can be modelled analytically considering that the screen is swept across its thickness by a plane to obtain the cross-sections of the threads that limit the size of the area of the pore.

2.1. Description of the problem

Easy measurements of geometric parameters (or desired values, if a specific design is intended), such as diameter of threads, separation between threads and thickness, allow the full geometric characterisation of a plain square woven/wire screen [14]. As depicted in Figure 1, the threads/wires are interlaced to form a complex structure. This means that the pore also has a complex volumetric shape, which has a very strong impact on the porous properties [39, 52, 66] and screening performance [31] of the screen. To calculate the pore-related parameters of a screen simply from few geometric data (or even directly from pictures [67]) is not straightforward, as there are no general equations that model the shape of the pore. The present work proposes a method based on sweeping the screen pore with a plane from the beginning to the end of its thickness. This sweeping allows the local area of the pore to be calculated as the difference between the total projected area and the intersection between the plane and the thread/wire shapes. Later, the discretisation approach to be introduced in this section allows the integration of the local variation of the area of the pore along the thickness to obtain the desired pore-related parameter.

2.2. Non-linear model of the structure of threads

Since the objective is the development of an analytical model for the variation of the area of the pore, a set of equations that describe the geometry of the interlaced threads must be introduced first. Peirce [68] introduced a model for cloth woven structures, which consisted on a total of seven equations that connect a total of eleven quantities:

$$c_i = \frac{l_i}{p_i} - 1, \tag{1}$$

$$p_i = (l_i - H\theta_i)\cos\theta_i + H\sin\theta_i \tag{2}$$

$$h_i = (l_i - H\theta_i)\sin\theta_i + H(1 - \cos\theta_i), \tag{3}$$

$$H = h_i + h_j, \tag{4}$$

where $i = x,y$ (this notation throughout the manuscript denotes the threads in the x-coordinate [x-threads or weft] and y-coordinate [y-threads or warp]), c_i is the crimp, l_i is the total length of each i-thread/wire, p_i is the horizontal spacing between the centre of the threads (from a 2D view) of i-threads/wires, θ_i is the inclination angle with respect to the plane parallel to the screen or contact angle, and h_i is the vertical separation of the centre of threads. A 2D sketch of this geometry is shown in Figure 2. This set of non-linear equations requires to know seven out of

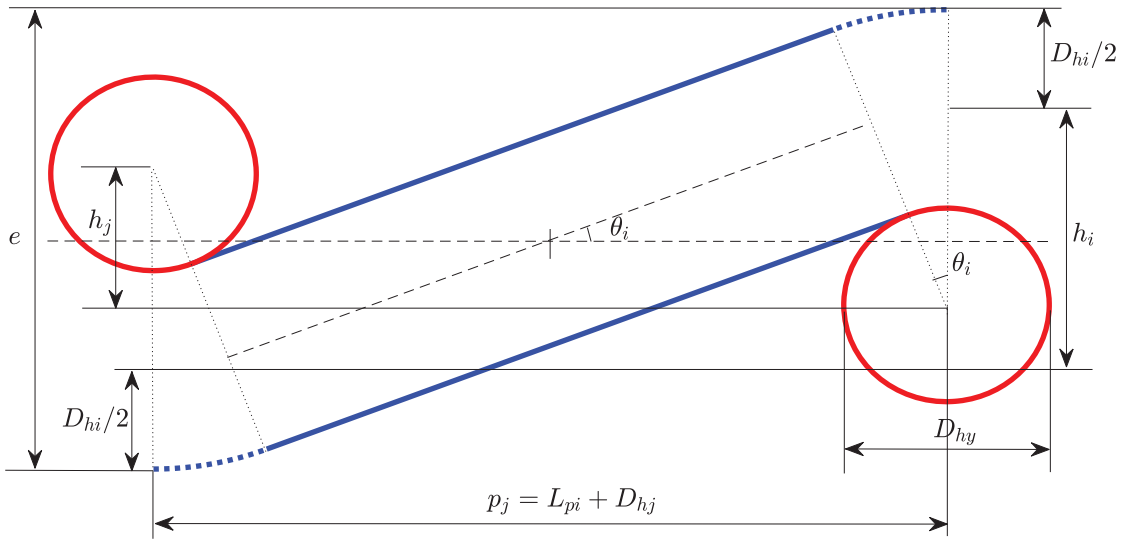

Figure 2: 2D Sketch of interlacing of threads/wires. The red threads (j-thread) represents the ones perpendicular to the view plane (of diameter D_{hj} and separated a L_{pi} distance horizontally in this view) and the blue threads (i-thread) are the transverse ones (of diameter D_{hi} and separated a L_{pj} distance). The contact area and inclination of threads is determined by the angle θ_i for the i-thread in this view.

eleven quantities to solve the geometry. Unfortunately, as said in [69], these equations are not solved easily, and researchers have attempted to solve, simplify or approximate them by means of different approaches. Moreover, to reconstruct the full geometry from real screens, it is important to ~~rely on~~ have realistic measurable quantities. ~~That is~~ In other words, quantities such as crimp, total length l_i, separations h_i or the θ_i angles are good options from theoretical viewpoint but not in practice. This is because they are not as easy to measure as other quantities such as the thickness e, the inner spacing between threads L_{pi}, and the diameter of threads D_{hi}. For this reason, from trigonometric relations, additional equations have been added in Granados et al. (2022) [14] to the set of non-linear equations:

$$h_i = (D_{hi} + D_{hj})(1 - \frac{1}{\cos\theta_i}) + (L_{pi} + D_{hj})\tan\theta_i. \tag{5}$$

$$h_j = \frac{(D_{hi} + D_{hj})}{\cos\theta_i} - (L_{pi} + D_{hj})\tan\theta_i, \tag{6}$$

However, these equations are not extendable to any WS, since there is dependence on the thickness e and the thread that constrains the thickness in asymmetric meshes (the diameter is not the same for all threads and the thickness is not twice the diameter). This can be solved by the aggregation of a categorical parameter, which is the type of configuration. If the WS is of type *Configuration 1* this means that in Figure 2 $i = x$, and the thickness e is measured as the distancing between the upper and bottom sides of the x-thread. *Configuration 2* would mean that $i = y$, and the y-thread define the thickness. This is translated into the equations:

$$\begin{aligned} h_i &= e - D_{hi}, \\ h_j &= 2D_{hi} + D_{hj} - e, \end{aligned} \tag{7}$$

Although by simply using the $i = x$,y notation (equivalent to rotate the mesh 90 degrees) the model would be valid for either x- or y-threads without the necessity of defining *Configuration 1* or 2, in the weaving of the WS structure it is important to define the warp and weft threads. In addition, in IPS in greenhouses it is usual to have pores longer in the y-direction, and the subscript of the thread is known beforehand. From the measured parameters, a solution to the full system of non-linear equations can be found, and this allows to obtain the 3D structure of the mesh, see Figure 3. In the figures can be seen that each interlaced thread/wire can be modelled as an inclined cylinder, whose top and bottom parts are joined to portion of toroidal volumes. Thus, from using the equations given in Equations (1)-(7), in combination to the parametric equations of a cylinder, a toroid, and a plane, one can parametrise the full pore and mesh geometries analytically.

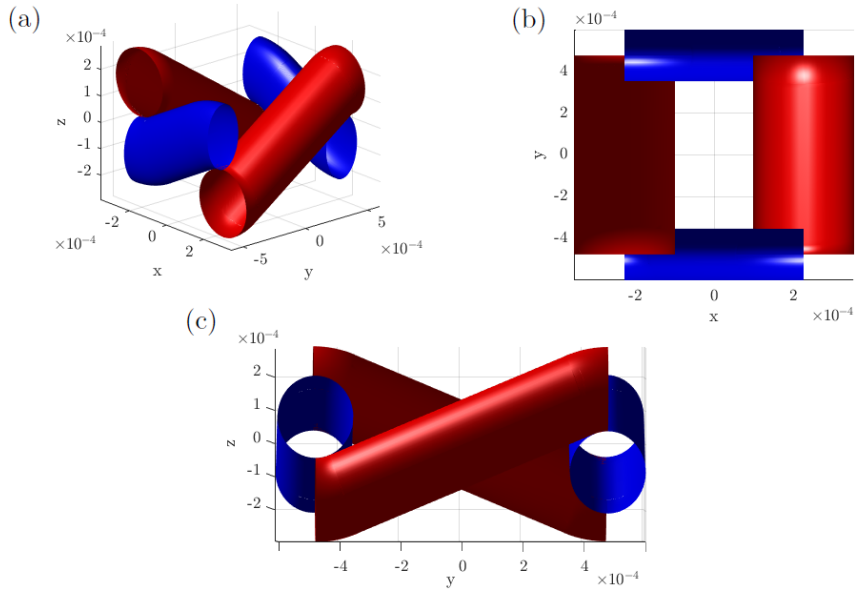

Figure 3: Different views of the 3D model generated from the solution of the non-linear equations. Mesh with *Configuration 2* (x-threads in blue, y-threads in red). The visualisations in the figure are: a) isometric view, b) top view (xy view), and c) side view (yz view). All units in meters.

2.3. Local variation of the cross-sectional area of a pore

When the plane parallel to the screen cuts the thread at a height such that both a portion of a torus and the inclined cylinder are sectioned, then the calculation of the cross-section areas is complex. This requires the calculation of the polar angles at which both the parametric curve of the cylinder and the portion of torus coincide. The calculation of these limiting angles can be explored in two different ways: 1) by creating a system of non-linear equations from the equality between the two said parametric curves (the solution would be the point of convergence), or 2) by some trigonometric work on the position of threads, which leads to non-linear equations. The latter option is less complicated from a mathematical viewpoint. The determination of the limiting polar angles to the solution of the area integrals[1] must be done separately for the cylinder and the portion of torus that make up the full thread. To obtain the cross-sectional area of the torus and cylinder dependent on z requires some mathematical elaboration and identification of possible scenarios (for instance, for the toroidal volumes, three different cross-sections will appear in a transversal intersection with a plane). Details on this are given in Appendix A.

[1]Please bear in mind that, despite the concept of surface integral is usually in mathematics referred to an extension of double integrals evaluated on surfaces, the definition of area integral is adopted in the present paper to denote the solution to integrals that represent areas.

To obtain the equations that model the local variation of the area of the pore, one has to bear in mind all the possible scenarios in the intersection between the plane and the mesh. ~~To this aim~~ To achieve this, we suggest to split the thickness of the screen into different parts or stretches $\mathcal{S}$. The different scenarios are illustrated in Figures 4 and 5. From these figures it is clear that when sweeping the thickness e from $z = e/2$ up to $z = 0$, we may have up to six different zones or stretches for any arbitrary i-thread and j as the transverse threads:

- Stretch 1: which corresponds to only intersections between the plane and an upper toroid (Figure 4(a)). This occurs for $z \in [e/2, (R_{hj} + D_{hi})\cos(\theta_i) - h_j/2$ (if the i-thread limits the thickness) or $z \in [(R_{hi} + h_i/2, (R_{hj} + D_{hi})\cos(\theta_i) - h_j/2$ (if the i-thread does not limit the thickness). If the both threads have the same size and limit thickness, thus the first relation is valid for both.

- Stretch 2: which corresponds to intersections between the plane and both a cylinder and an upper toroid, constrained also by the vertical symmetry axis of the toroid section (Figure 4(b)). This occurs for $z \in [(R_{hj} + D_{hi})\cos(\theta_i) - h_j/2,\ R_{hj} - \frac{h_j}{2})$.

- Stretch 3: which corresponds to intersections between the plane and both a cylinder and an upper toroid, but this time constrained by the "inner hole" of the toroid (z delimited between Figure 4(c) and 4(d)). When it appears, this usually occurs for $z \in [R_{hj} - \frac{h_j}{2},\ R_{hj}\cos(\theta_i) - h_j/2)$.

- Stretch 4: which corresponds to intersections between the plane and a cylinder only. When it appears, this usually occurs for $z \in R_{hj}\cos(\theta_i) - h_j/2,\ h_j/2 - R_{hj}\cos(\theta_i)]$.

- Stretch 5: which corresponds to intersections between the plane and a cylinder, an upper toroid and a bottom toroid (Figure 5(a)). In this Stretch, the upper toroid is constrained as in Stretch 2. However, the bottom toroid cross-section is constrained by the "inner hole". The cross-section of the cylinder is delimited by the contact with two toroids. When it appears, this usually occurs for $z \in [h_j/2 - R_{hj}\cos(\theta_i),\ h_j/2 - R_{hj})$.

- Stretch 6: which again corresponds to intersections between the plane and a cylinder, an upper toroid and a bottom toroid (Figure 5(b)). Again, in this stretch, the upper toroid is constrained as in Stretch 2. However, the bottom toroid section is constrained by the vertical

symmetry axis of the toroid section. The cross-section of the cylinder is again delimited by the contact with two toroids. When it appears, this usually occurs for $z \in [h_j/2 - R_{hj},\ 0]$.

It is very important to emphasize that the appearance of each of the six stretches is rare. Depending on the shape of the interlacing of threads, some stretches may not ~~be present~~ exist. For instance, for a fully symmetric mesh (same diameter for all threads, thickness equal to two times the diameter) only Stretch 1 and 2 will appear, for both the warp (y-thread) and weft (x-thread) threads. However, for the threads analysed in the present paper, which correspond to usually very non-symmetric configurations, it is usual to see Stretches 1, 2, 3 and 4 for the warp thread; and Stretches 1, 2, 5 and 6 for the weft threads (see example in Figure 6). The appearance/disappearance of these stretches also may vary the lower limits in the above-given description of each stretch. That is to say, depending on the position of the $z = 0$ plane in the thread geometries, some of the given limits would be negative. In this scenario, the integration limits for z at each stretch should be adapted to the next limit (these limits abovementioned are named as zp_q^x and zp_q^y, with $q = 0, ..., 5$ in Appendix B). The numerical code in AeroScreen software does this automatically. In addition, due to symmetry, the same intersections between the plane parallel to the screen and the threads will be found for $z \in [-e/2,\ 0]$, and $z \in [0,\ e/2]$, thus only one half will be integrated.

For the first four stretches, which only involve the upper toroid portion, the delimitation of which parts to consider from the cross-sections from the portion of torus and the cylinder are given by the $C1$ and $C2$ points (point C in the 2D representation in Figure 7), which corresponds to the intersection between their parametric curves. In Figure 7, it is provided an example of calculation of limits for a thread positioned parallel to the Z-Y plane. It can be observed that the y-position of the intersection between the plane and the separation region between the cylinder and the torus happens at a distance $y_{lim} = O_y - d$ to the center of coordinates, where the y-axis position of the thread below is $O_y = (L_{pi} + D_{hj})/2$ and $d = (z' + h_j/2)\tan(\theta_i)$. Thus, by equalising $y(s)$ with such distance and using z as z-coordinate for z' (for the sake of notation hereinafter), we obtain a non-linear equation, with solutions

$$\begin{aligned} s^i_{lim}(z) &= \sin^{-1}\left(\frac{z\cos(\theta_i) - y_{lim}\sin(\theta_i)}{R_{hi}}\right), \\ s^i_{lim}(z) &= \pi - \sin^{-1}\left(\frac{z\cos(\theta_i) - y_{lim}\sin(\theta_i)}{R_{hi}}\right). \end{aligned} \tag{8}$$

The first of these two solutions is preferred because it falls into an appropriate quadrant, and the area integrals will be solved in such. Once the polar angle limit is available, the cross-sectional

area of the cylinder can be calculated based on the limiting angles by the torus as:

$$A_{cyl}(z) = 2\int_{s^i_{lim}(z)}^{\pi/2} (R_{hi}\cos(s))\left(\frac{R_{hi}\cos(s)}{\sin(\theta_i)}\right) ds = \frac{2R^2_{hi}}{\sin(\theta_i)}\left[\frac{1}{2}(s+\sin(s)\cos(s)\right]_{s^i_{lim}(z)}^{\pi/2}. \quad (9)$$

From the solution to this integral, it is clear that the cross-section of the inclined cylinder with respect to the plane parallel to the screen is constant (always an ellipse). The dependence on z is only dictated by $s_{lim}(z)$ due to the intersection with the cross-section of the torus.

Similarly, this can be done for the torus section. However, must be taken into account that for the four stretches shown in Figure 4, there are two limiting values for the polar angle v in the parametric equations given in Equation (A.2): one for the vertical symmetry plane of the torus, and one for the contact area between the torus and cylinder (as seen in the calculation of $s^i_{lim}(z)$).

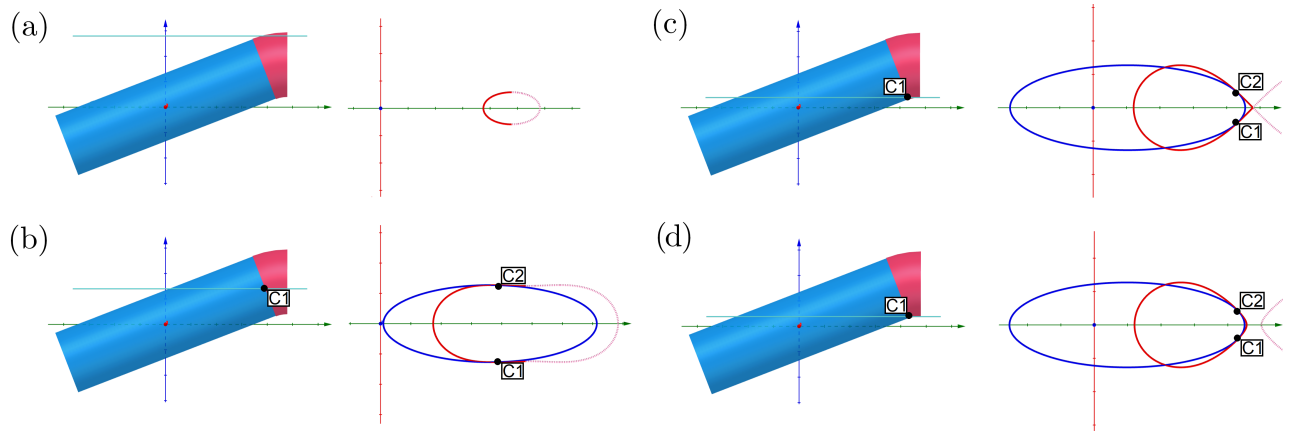

Figure 4: Different full cross-sections obtained when the plane parallel to the screen (green horizontal line) cuts the torus portion at different heights: a) Only torus, b) Torus and cylinder at intermediate distances (single deformed oval curve), c) Torus and cylinder at z tangent to the j-thread hole top (lemniscate-like curve), and d) Torus and cylinder when intersecting the "inner hole" of the torus (two ovals). The full elliptic curve of the cylinder is also shown in blue for reference for the limiting points $C1$ and $C2$.

For the first case, ~~to obtain the limit angles, the limit value of v can be considered the value of v that would lead to~~ the limiting angles are calculated by using the limiting value of v which itself leads to a constant value of $y(v) = (L_{pi} + D_{hj})/2$. This can be, for the sake of simplicity, translated to $y = 0$. The solution v to this non-linear equation is:

$$v^i_{lim1}(z) = \pi \pm \cos^{-1}\left(\frac{a \pm z \mp O_z}{R_{hi}}\right), \quad (10)$$

with $a = (D_{hi} + D_{hj})/2$, and one can select the following real value in a suitable quadrant:

$$v^i_{lim1}(z) = \pi - \cos^{-1}\left(\frac{a - z + O_z}{R_{hi}}\right). \quad (11)$$

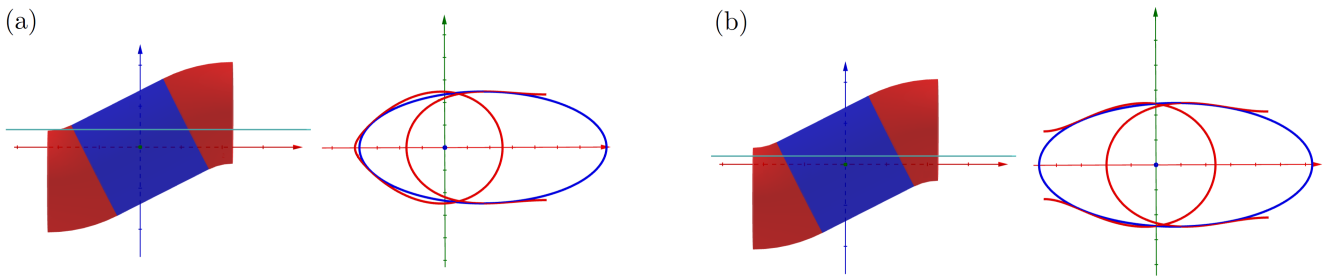

Figure 5: Full cross-sections involving both the upper and bottom toroid portions. a) Upper toroid portion delimited by the vertical symmetry axis and bottom toroid portion delimited by the inner hole. b) Both upper and bottom toroid portions delimited by their vertical symmetry axes.

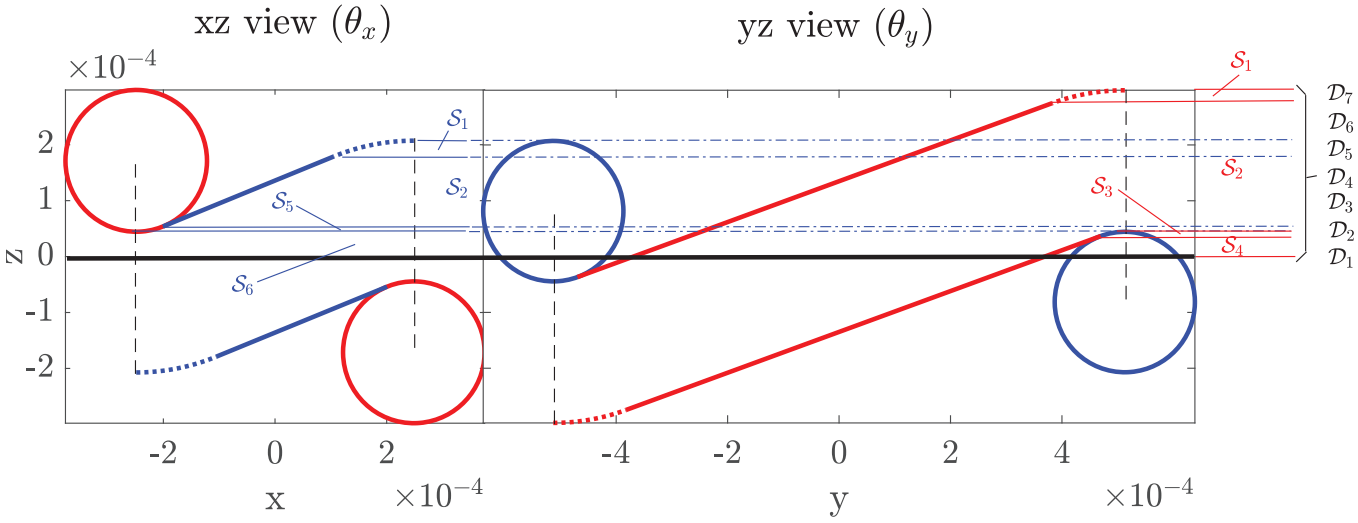

Figure 6: Stretches for an specific mesh with *Configuration* 2 ($N_{WS} = 11$). Warp threads are shown in red, and weft in blue. It can be observed all the stretches $\mathcal{S}$ that lead to the definition of the seven Discretisations $\mathcal{D}$. Both xz and yz views are placed together for better comprehensive interpretation of the definition of the Discretisations. Stretches from the xz view are extended by means of dashed lines to overlap all the stretches at the right hand-side for better identification of Discretisations. The horizontal black thick line represents $z = 0$, as only one half is analysed due to symmetry. All units are in meters.

Similarly, for the second limit value one has to solve the non-linear equation resulting from making equal $y(v)$ in Equation (A.2) and y_{lim}, according to the geometry shown in Figure 7), which yields the following limit value of v:

$$v^i_{lim2}(z) = \pi \pm \cos^{-1}\left(\frac{a \pm \sqrt{d^2 + (z - O_z)^2}}{R_{hi}}\right). \tag{12}$$

Amongst these solutions (some may lead to complex values), one can get the real value:

$$v^i_{lim2}(z) = \pi - \cos^{-1}\left(\frac{a - \sqrt{d^2 + (z - O_z)^2}}{R_{hi}}\right). \tag{13}$$

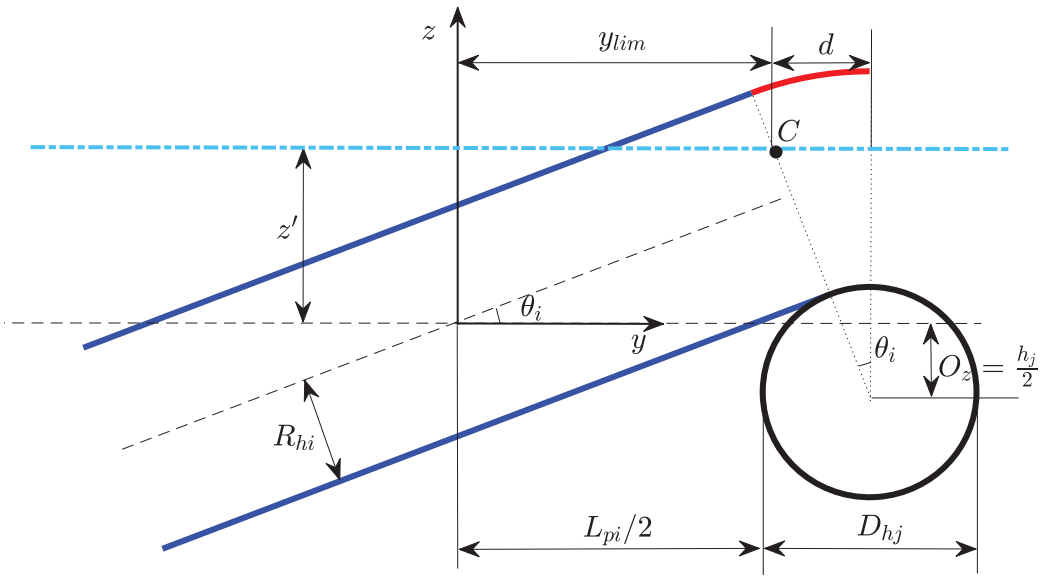

Figure 7: 2D sketch of the full thread cut intersected by a plane parallel to the screen at $z = z'$. y_{lim} defines the horizontal position of the limiting point denoted as C for the sake of planar notation, but which in reality stands for the two points $C1$ and $C2$ in three dimensions.

For the transverse threads, j, the limits are studied in the x-axis, thus y_{lim} would actually be x_{lim}. We preferred to focus on a particular y-axis notation rather than using more sub-indices in order to avoid confusing the reader with an overload of notation.

Finally, a scenario in which both the upper and bottom toroid portions are intersected by the plane may take place. This situation is depicted in Figure 5. In Figure 5(a) is illustrated an intersection in Stretch 5. All cross-sections in this stretch include a bottom toroid, which is delimited by the inner hole, that is, by the shape of the toroid itself, and the joint with the cylinder.

To obtain the limit value of the angle v in the equations of the bottom toroid portion (bt), one has to solve the non-linear equation resulting from making equal the equation of the bottom toroid and $-y_{lim2}$, where $y_{lim2} = O_y - d_2$, and $d_2 = (h_j/2 - z)\tan(\theta_i)$. This is almost the same concept as in the calculation of $v^i_{lim2}(z)$. This calculation leads to the analytical solutions:

$$v'^{\,i}_{\,lim2}(z) = \pi \pm \cos^{-1}\left(\frac{a \pm \sqrt{d_2^2 + (z + O_z)^2}}{R_{hi}}\right). \tag{14}$$

Amongst these four solutions, the one of interest is the one from the quadrant:

$$v'^{\,i}_{\,lim2}(z) = \pi - \cos^{-1}\left(\frac{a - \sqrt{d_2^2 + (z + O_z)^2}}{R_{hi}}\right). \tag{15}$$

In this stretch, the cross-section of the cylinder is delimited at both the left and right sides by the joints with the toroid portions. Thus, there are two limits for the area integral: the $s^i_{lim}(z)$ already

explained for the joint with the upper toroid, and a new $s^i_{lim2}(z)$ for the bottom toroid joint. This limit for the integration is obtained in a similar manner to $s^i_{lim}(z)$ in Equation (8). This time, it is the equation of the bottom toroid portion the one which must be set equal to the negative values at the limit with the cylinder, $-y_{lim2}$. As there are two intersection points between the toroid and the cylinder, there are two solutions:

$$\begin{aligned} s^i_{lim2}(z) &= \sin^{-1}\left(\frac{z\cos(\theta_i) + y_{lim2}\sin(\theta_i)}{R_{hi}}\right), \\ s^i_{lim2}(z) &= \pi - \sin^{-1}\left(\frac{z\cos(\theta_i) + y_{lim2}\sin(\theta_i)}{R_{hi}}\right). \end{aligned} \tag{16}$$

The first solution is preferred, due to this corresponds to a quadrant positive integration. There is no need to use both solutions as there is symmetry. Once the polar angle limit is available, the cross-sectional area of the cylinder can be calculated by using the limiting angles $s_{lim}(z)$ and $s_{lim2}(z)$.

The last scenario is illustrated in Figure 5(b), which corresponds to Stretch 6. The cross-section of the cylinder and the upper toroid is the same, but the bottom toroid *bt* has its cross-section limited by the joint with the cylinder (as Stretch 5) and by the symmetry axis. This limit for the integral at the vertical symmetry axis is obtained from making equal $y_{bt}(v)$ and $-O_y$, whose solution is:

$$v'^{\,i}_{lim1}(z) = \pi \mp \cos^{-1}\left(\frac{a \pm z \mp O_z}{R_{hi}}\right), \tag{17}$$

and it is chosen the following value corresponding to the suggested quadrant integration:

$$v'^{\,i}_{lim1}(z) = \pi - \cos^{-1}\left(\frac{a + z + O_z}{R_{hi}}\right). \tag{18}$$

2.4. Integration of the area of the pore along the thickness. Calculation of the constriction factor and volume of pores

The analysis developed in the previous sections was based on the interaction of a plane parallel to the screen with a single thread. This idea can be exported to an WS taking into account that this is made of four threads per pore (two threads in the x-coordinate direction, of diameter D_{hx}; and two threads in the y-coordinate direction, of diameter D_{hy}). However, this is not an easy task due to several reasons. First, the angle of the threads in the x-direction (namely x-threads or weft), θ_x, and in the y-direction (namely y-threads or warp), θ_y, as well as their lengths, is not the same. Actually, the geometry of the interlaced of threads is quite complex, as discussed in [14], being dependent on the separation of the threads (L_{px} and L_{py}), their diameter (D_{hx} and D_{hy}), the

thickness (e), and their structure (*Configuration 1* or *2*). Second, and related to the first point, due to the different geometries that present each thread, when the plane intersects one thread at a certain stretch, it is very likely that the transverse threads will not be intersected at the same stretch, due to the different height of each thread (see Figure 6). Thus, the sweeping of the plane on the insect-proof mesh structure must be done carefully, depending on the mesh shape.

The integration of the area of the pore along the thickness is of interest to calculate descriptive parameters that characterise the mesh, as for instance volumetric porosity or the constriction factor. The calculation of the integral of the area of the pore through the mesh (volume of the pore) and the inverse allows to perform the full calculation of the constriction factor, given by

$$CF = \frac{1}{e^2} \int_{-e/2}^{e/2} A_p(z)dz \int_{-e/2}^{e/2} \frac{1}{A_p(z)} dz, \tag{19}$$

which is a parameter that estimates the effectiveness of the pore to conduct the flow [60]. A larger value of CF reflects a reduced ability to let the flow pass from the inlet of the pore to the outlet. The first integral in Equation (19) is equivalent to the volume of the pore V_p, which is:

$$V_p = \int_{-e/2}^{e/2} A_p(z)dz = 2 \int_{0}^{e/2} A_p(z)dz. \tag{20}$$

This integral can be solved taking into account the suggested approach stretch by stretch. This method consists of decomposing A_p in the integral of Equation (20) into the different areas along the stretches introduced in Section 2.3:

$$V_p = \int_{-e/2}^{e/2} \left[A_t - (A_x(z) + A_y(z))\right] dz = V_t - \left(\int_{-e/2}^{e/2} A_x(z)dz + \int_{-e/2}^{e/2} A_y(z)dz \right), \tag{21}$$

where the areas of the x-thread ($A_x(z)$) and y-thread ($A_y(z)$) are obtained and integrated for each stretch. The method is explained in detail in Appendix B. For validation purposes, the result from this integration can be compared to the volumetric porosity calculated in [14]. Since in [14] the volumetric porosity is calculated as the percentage of volume of the threads over the total volume, the volume of the pore can be computed as

$$V_p = V_t \, \phi_{3D}, \tag{22}$$

where the total volume is calculated as $V_t = (L_{px} + D_{hy})(L_{py} + D_{hx})e$, and ϕ_{3D} is calculated with the Poro3D software [70]. Results have been validated with Equation (22) for the 20 WSs analysed in [14] and the difference is negligible, with an average error of $O(10^{-20})$.

Therefore, the first integral in Equation (19) can be solved by decomposition of A_p with respect to z (the actual volume of the pore V_p) into several terms related to the intersection of the plane with the x- and y-threads. However, regarding the second integral in Equation (19), the decomposition approach in Appendix B is not possible, as $A_p(z)$ is in the denominator and the integration of $1/A_p$ cannot be decomposed under the same reasoning. This complicates the problem substantially, since as aforesaid, the area from the intersection between a torus and an horizontal plane has no solution in terms of elementary functions. This leads to a complex multidimensional integral: depending on the z position, each thread may be into a different stretch (see Figure 6), and the limits of the integrals will be different for each area at each z position. In addition, depending on the stretch, the horizontal plane may encounter e.g. a piece of torus in an x-thread, whereas may encounter a cylinder+piece of torus for the y-thread. The impossibility of decomposing the integral into terms related to each thread, complicates the identification of a solution to the problem.

To overcome these difficulties, we propose a methodology based on a discretisation from a re-grouping of the proposed stretches, in order to solve piece-wise integrals. In other words, this methodology consists of discretising the integration interval with z into different integrals from the combination of all the stretches. Thus, each integral is solved independently. ~~Opposite~~ In contrast to the approach introduced in Appendix B for the volume of the pore, this allows to work with all threads at the same time. Thus, the first integral in Equation (19), besides by using Equation (22), can be calculated either according to Appendix B or by means of the discretisation approach. The results are identical.

From the combination of all the stretches $\mathcal{S}_k$ for each thread, the new discretisation of $z \in [0, e/2]$ into different $\mathcal{D}_m$ intervals (called hereinafter discretisations), with $m = 1, 2, ..., n$, is $[0, e/2] = \mathcal{D}_1 + \mathcal{D}_2 + ... + \mathcal{D}_n$. For an arbitrary discretisation $\mathcal{D}_m$, the area of the cross-section of the x-thread with the horizontal plane ($A_{\mathcal{S}_{\mathcal{D}m}x}(z)$) is selected according to its stretch $\mathcal{S}_{\mathcal{D}m}$. This is extendable to the cross-section of the y-thread, $A_{\mathcal{S}_{\mathcal{D}m}y}(z)$, so that one can obtain:

$$\int_{-e/2}^{e/2} \frac{1}{A_p(z)} dz = 2\int_{0}^{e/2} \frac{1}{A_p(z)} dz = 2\int_{0}^{e/2} \frac{1}{A_t - (A_x(z) + A_y(z))} dz = 2\left(\int_{\mathcal{D}_1} \frac{1}{A_t - (A_{\mathcal{S}_{\mathcal{D}1}x}(z) + A_{\mathcal{S}_{\mathcal{D}1}y}(z))} dz + \int_{\mathcal{D}_2} \frac{1}{A_t - (A_{\mathcal{S}_{\mathcal{D}2}x}(z) + A_{\mathcal{S}_{\mathcal{D}2}y}(z))} dz + ... + \int_{\mathcal{D}_n} \frac{1}{A_t - (A_{\mathcal{S}_{\mathcal{D}n}x}(z) + A_{\mathcal{S}_{\mathcal{D}n}y}(z))} dz\right). \quad (23)$$

This piece-wise integration is not easy, as the resulting integrals are not strictly double or triple integrals, but nested ($A_{\mathcal{S}_{\mathcal{D}m}x}(z)$ and $A_{\mathcal{S}_{\mathcal{D}m}y}(z)$ are actually integrals, whose integration limits also depend on z, see explanation of stretches in the previous section). The identification of the integrals

and the selection of each area per stretch (that is, $A_{\mathcal{S}_{\mathcal{D}m}x}(z)$ and $A_{\mathcal{S}_{\mathcal{D}m}y}(z)$) to be integrated with respect to z is done in the same way as described in Appendix B. An example of discretisations from the case scenario ~~shown in Figure 6~~ are given in Figure 6, which shows a total of seven discretisations.

3. Results and Discussion

The discretisation method has been applied to real symmetric wire screens studied in previous works [44, 66, 71], to validate the results and observe differences in the calculation of the constriction factor as well as in the calculation of the volumetric porosity. Also, the discretisation method has been applied to a set of 20 real woven screens (WSs) with asymmetric mesh frequently installed in Mediterranean greenhouses to spot differences with the estimation of porosity via volume integration of toroid and cylinder done in Granados et al. (2022) [14].

3.1. Validation of the modelling with symmetric wire screen data

The only previous work in the literature on the estimation of the constriction factor was done by Wang and coworkers [66]. In this work, a formula to calculate this parameter is proposed for several types of mesh, including the one under study in this work (named as *plane square* screen in [66]). However, their investigation has serious drawbacks. First, their calculation is based on the assumption of strong linear variation of the area of the pore with z, as shown in Equation (24):

$$A_p(z)^{linear} = (L_p + D_h)^2 - \frac{2B}{D_h}z, \tag{24}$$

where L_p is the separation between threads, D_h is the diameter of threads, and $B = \frac{\pi D_h(L_p+D_h)}{4}$. This leads to an important simplification specially in non-symmetric meshes. The construction of their $A_p(z)/A_t$ plots (A_t is the projected total area of the pore) to interpolate or approximate with a linear approach is also unclear, possibly constructed from image detection. Second, the formula provided is only tested for fully symmetric screens ($D_{hx} = D_{hy} = D_h$, $L_{px} = L_{py} = L_p$, $e = 2D_h$), so the efficacy for very distorted meshes is unknown. The evolution of the local area of the pore A_p from the upper side to the bottom side of the mesh must be analysed to validate that results and the approach are correct. When modelling it, one has to check whether the solution is feasible, since when approaching $z = 0$ a horizontal is expected to ensure symmetry in both half of the thickness. To achieve this, our approach has been compared to the linear approximation as depicted in Figure 8 for two screen meshes: a fully symmetric mesh (same diameter for all threads,

thickness equal to two times the diameter), for which only Stretch 1, 2 and 5 will appear; ~~a typical configuration;~~ and a asymmetric screen mesh, for which 6 stretches exist. The figure shows the evolution of the area of the pore at each z position (made dimensionless with the total area) and the area occupied by each yarn at each z position and its corresponding stretch.

The linear approximation suggested by Wang et al. (2021) [66] is far from reality for non-symmetric meshes, as seen in Figure 8, where a linear approximation following the reasoning in Wang et al. is intended to show the difference in the trend for non-symmetric meshes. It is also noticed that the use of a linear approximation leads to a non-differentiable plot for A_p in $z = 0$. The change from positive values of z to negatives is abrupt, which is not consistent with reality.

Table 1 shows a comparison between constriction factor and volumetric porosity (both calculated from the integration of the expression of the linear approximation for the variation of area of the pore shown in Equation (24)) from fully symmetric meshes in Figure 8 and the current proposed method. Porosity is also validated with experimental data from the literature. In the table can be observed that whilst in the calculation of the constriction factor the differences between the linear approximation and the proposed discretisation method is not large, in the calculation of porosity the difference is more remarkable. Compared to the experimental results reported in the literature, the discretisation method provides a more accurate estimation of porosity, specially when the thread density is increased. This makes sense, as in meshes with small pore sizes the presence of threads is more notorious. In large separation between threads a mesh has less dependence on the interlacing threads and even on thickness. Nevertheless, ~~must be recall~~ it must be stressed that these results are related to fully symmetric meshes as they are the only data available in previous literature for the constriction factor. For asymmetric meshes the difference would be greater as will be seen next.

3.2. Calculation and validation of the volume of the pore and constriction factor for different measured asymmetric screens

The discretisation method has been applied to a total of 20 WSs from Granados et al. (2022) [14]. Table 2 and Figure 9 show the results from the calculation of the constriction factor with Equation (19). The results are validated with the calculation of the volume of the pore V_p via Equation (22) (V_p from ϕ_{3D}) and discretisation method (V_p Current). The match has a negligible difference, an absolute average error of $O(10^{-20})$, due to the adaptive quadrature method to solve the definite nested integrals for which there is no solution in terms of elemental functions.

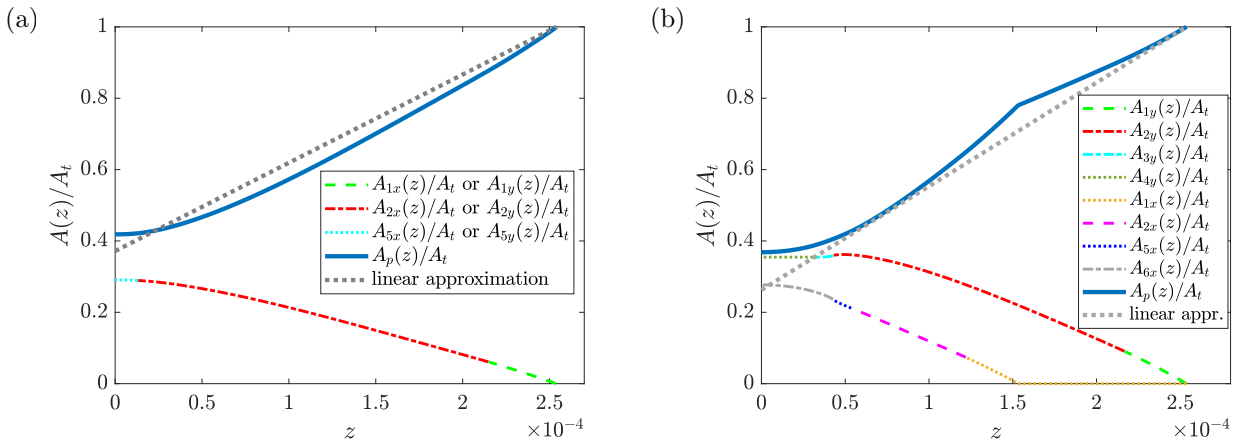

Figure 8: Plots of the analytical estimation of the area of the pore with z and cross-sectional areas of the threads/wires $A_{\mathcal{S}_{Dm}x}(z)$ and $A_{\mathcal{S}_{Dm}y}(z)$ from the intersection by the plane for each Stretch $\mathcal{S}_{Dm}$ present. The dashed lines represent the linear approximation by Wang et al. [66]. The results are made dimensionless with the total projected area A_t and shown for: a) Fully symmetric mesh ($\rho_t = 40 \times 40$ in [66]), and b) Notably asymmetric mesh ($N_{WS} = 17$ in [14]). All units are in meters.

ρ_t[wires/inch^2], D[m]	CF^{linear}	CF	ϕ_{3D}^{linear}	ϕ_{3D}	ϕ_{3D} exp.
4×4, $D = 5.1E-4$	1.0015	1.0019	0.937	0.936	0.919 [44]
40×40, $D = 2.54E-4$	1.080	1.076	0.686	0.659	0.662 [71]
60×60, $D = 1.905E-4$	1.122	1.106	0.646	0.607	0.612 [71]
150×150, $D = 6.604E-5$	1.074	1.072	0.694	0.669	0.671 [71]

Table 1: Comparison of constriction factors and volumetric porosity for symmetric meshes. The calculation of the constriction factor via the present approach (CF) is compared with the linear approximation (CF^{linear}), and the estimation of porosity experimentally (ϕ_{3D} exp.) is compared to results via Discretisation Method (ϕ_{3D}) and by linear approximation (ϕ_{3D}^{linear}).

~~In addition, it is useful to observe the evolution of the local area of the pore from the upper side to the bottom side of the mesh in a plot. This allows to check whether the solution makes sense or not, since when approaching $z = 0$ a horizontal is expected to ensure symmetry. This is depicted in Figure 8 for two WSs: a fully symmetric mesh (same diameter for all threads, thickness equal to two times the diameter), for which only Stretch 1, 2 and 5 will appear; a typical configuration; and a asymmetric screen mesh. The figure shows the evolution of the area of the pore at each z position (made dimensionless with the total area) and the area occupied by each yarn at each z position and its corresponding stretch.~~ [Moved to previous section]

Must be outlined that the constriction factor is a value ideally close to 1 (an exact value of

N_{WS}	ρ_t	L_{px}	L_{py}	D_{hx}	D_{hy}	e	ϕ_{2D}	ϕ_{3D}	V_p (from ϕ_{3D})	V_p (DM)	CF
1	14 × 27	131.84	570.46	209.6	225.74	489.82	0.270	0.655	8.947E-11	8.947E-11	1.113
2	14 × 27	141.8	615.93	214.81	221.73	514.28	0.288	0.688	1.068E-10	1.068E-10	1.091
3	14 × 27	187.33	543.47	186.45	183.97	417.75	0.379	0.723	8.189E-11	8.189E-11	1.063
4	14 × 27	188.4	591.6	184.1	184.7	401.7	0.385	0.721	8.378E-11	8.378E-11	1.061
5	10 × 20	233.7	734	276.4	273.4	563.8	0.335	0.664	1.919E-10	1.919E-10	1.082
6	10 × 20	226.87	681.08	256.83	243.52	566.62	0.349	0.709	1.773E-10	1.773E-10	1.071
7	10 × 20	238.57	745.95	272	261.24	564.4	0.350	0.688	1.975E-10	1.975E-10	1.074
8	10 × 20	239.99	761.46	263.95	261.81	534.67	0.354	0.677	1.864E-10	1.864E-10	1.073
9	10 × 20	232.48	760.74	233.06	253.08	544.35	0.366	0.715	1.879E-10	1.879E-10	1.068
10	10 × 20	252.74	746.43	258.95	255.66	639.22	0.368	0.745	2.435E-10	2.435E-10	1.058
11	10 × 20	243.71	773.99	251.59	253.5	595.82	0.369	0.734	2.229E-10	2.229E-10	1.061
12	10 × 20	250.31	865.1	264.6	260.28	610.55	0.375	0.736	2.592E-10	2.592E-10	1.058
13	10 × 20	234.9	838.7	245.8	248	525.91	0.375	0.711	1.957E-10	1.957E-10	1.064
14	10 × 20	253.89	784.27	250.54	253.49	586.68	0.379	0.735	2.264E-10	2.264E-10	1.060
15	10 × 20	256.6	736.4	256.8	243.7	480.19	0.379	0.674	1.609E-10	1.609E-10	1.061
16	10 × 20	246.76	877.27	233.8	236.45	545.95	0.402	0.752	2.204E-10	2.204E-10	1.050
17	15 × 30	107.52	456.34	195.99	211.07	507.52	0.237	0.663	6.989E-11	6.989E-11	1.117
18	13 × 30	110.02	611.88	187.7	209.4	458.13	0.263	0.667	7.808E-11	7.808E-11	1.107
19	13 × 30	170.9	876.8	163.3	160	406.07	0.437	0.795	1.111E-10	1.111E-10	1.031
20	15 × 30	221.6	548.8	110.5	109.9	260.57	0.556	0.830	4.728E-11	4.728E-11	1.021

Table 2: Estimation of porosity and constriction factor for the 20 representative WSs studied in Granados et al. [14]. All units are given in micrometers (10^{-6} meters), but the volumes V_p in cubic micrometers. All screens are interlaced according to *Configuration 2*. N_{WS} is the number of woven screen, and the volume of the pore is calculated from the volumetric porosity in [14] [V_p (from ϕ_{3D})] and by the here introduced Discretisation Method [V_p (DM)]. The negligible difference in the comparison shows that the calculation of CF is very reliable via the DM.

unity would express that the area of the pore is constant [independent on the position z]). A mesh is more prone to have greater CF if the size of the pore is distorted and small in comparison to the area covered by the threads. A hint for this is how close the area occupied by the threads is to the total area of the pore A_p (A_x and A_y actually approaches or surpass A_p in the surroundings of $z = 0$). Another indicator can be the superficial porosity (ϕ_{2D}), whose relation can be observed in Figure 9. Although this can suggest certain degree of relationship, the superficial porosity is not a good indicator of correlation, since the thickness also plays an important role in the CF, and the thickness is not taken into account in the calculation of superficial porosity. This is observed also in Figure 9: whereas the superficial porosity is ordered from lower to higher grouped by density of threads (ρ_t), the CF is not varying with the same intensity. Actually, for meshes with $\rho_t = 10 \times 20$ the change is not highly noticeable and it is not monotonically incresing or decreasing. In general, the variability in CF is mild compared to the variability in porosity. ~~This actually suggest that the variability in CF, a parameter that has not yet been considered in computational models of ventilation of vents with IPSs [39], may account a correction to errors in the aerodynamic behaviour of IPSs worthy of consideration. Models in the literature [39] actually mimic very poorly pressure~~

~~drop and inertial factor of IPS because of a lack of 3D structural properties [14].~~

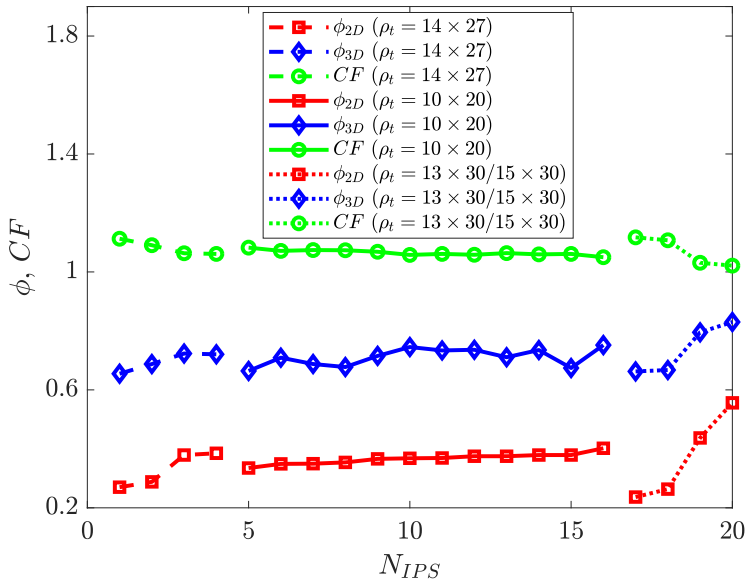

Figure 9: Superficial porosity (ϕ_{2D}), volumetric porosity (ϕ_{3D}), and constriction factor (CF) for each screen. Screens are grouped by density of threads (ρ_t in [threads/cm^2]) and ordered from low to high superficial porosity.

In order to gain more knowledge on the effect of the geometry on pore-related properties (constriction factor, porosity and local area of pores), the One-factor-At-a-Time (OAT) method [72] has been carried out. The asymmetric $N_{WS} = 17$ screen has been selected as baseline design, which will need to be re-designed. On this screen, two design space dimensions have been explored by varying one of the design parameters and keeping the other fixed to their baseline value: one of the diameters, D_{hx}, has been varied from a 50% up to a 110% of the original baseline value; and the thickness e has been varied from a 90% up to a 120% of the original baseline value. Wider ranges are not possible because values outside these limits lead to unfeasible (unrealistic) geometries. In other words, there is no solution to the set of nonlinear equations given in Equations (1)-(7). The separation of the threads (L_{px} and L_{py}) has not been explored by OAT, since in principle the separation can be increased a lot while still obtaining feasible geometries. This leads to a continuous increase (decrease) in porosity (constriction factor), and the challenge is actually to restrict the screen to a certain pore inner diameter that blocks certain size insects/objects and to vary mostly diameters&thickness to achieve the best screen. Also, depending on the application, engineers may intend a specific design to suit a specific pore size, porosity and/or constriction factor.

As seen in Table 3, when increasing D_{hx}, the constriction factor was increased from a $CF = 1.0498$ up to a $CF = 1.1288$, and porosity was decreased from $\phi_{3D} = 0.7249$ up to $\phi_{3D} = 0.6433$. The explanation behind this increase in the constriction factor is that, as the diameter of the wire is increased, the volume occupied by the wire is increased (actually, the thread is also increasing its inclination and elongation to fit in the new geometry [always a *Configuration 2* one], as can be seen in the top figure in Figure 10(a)). This affects to the local cross-sectional areas of the pore at the different z locations by creating more "distorted" pore volume geometries (see Figure 10(b) to observe that for larger values of D_{hx} the impact of A_x on A_p is more remarkable). As the constriction factor is a parameter that estimates the ability of the pore to conduct the flow (also known as a fluctuation in local hydraulic radii) [60], it is clear that the more distorted the pore is, the greater the constriction factor (which should ideally be strictly equals to unity). In terms of porosity, the effect of increasing the diameter of the thread is clear: as all parameters but D_{hx} are fixed to their baseline value, the volume of the pore is decreased whilst the total volume is still the same. Therefore, the porosity decreases as the diameter of the wire increases.

Table 3 shows that, when increasing e, the constriction factor increases from a $CF = 1.1297$ up to a $CF = 1.0716$. Porosity is increased from $\phi_{3D} = 0.6449$ up to $\phi_{3D} = 0.7088$. In the event of searching for a new design by increasing the thickness e of the screen, opposite to the scenario when increasing D_{hx}, for the *Configuration 2* screen the x-threads tend to decrease their inclination as the y-threads increase their inclination (see Figure 11(a)) to keep delimiting the thickness of the screen (up to a point at which the only option to keep increasing the thickness would be to also increase D_{hy}). This has an easily predictable effect on porosity: the volume of the pore is increased whilst the volume of the wires is essentially the same (it varies very little, as the nearly negligible increases in length in the y-thread are cancelled by decreases in the x-thread). Thus, porosity is increased. The effect on the constriction factor is not that clear. When the thickness is increased, the x-threads are re-adapted to the geometry tending to a horizontal wire. That is why the A_x/A_t plot in Figure 10(b) tends to an ellipse and the A_p/A_t plot tends to look like a "curved step" (x and y-threads are swept in tandem). The y-threads increase their inclination, but more gently. Thus, it is hard to extract a conclusion from the behaviour of the threads. However, the terms in Equation (19) give a hint on the sensitivity of this factor to each parameter. It can be observed that the thickness has squared inverse relation to CF, thus this evokes that an increase on the thickness should dramatically reduce the constriction factor. But the limits of the integrals

% of D_{hx}	CF	ϕ_{3D}
50%	1.0498	0.7249
70%	1.0752	0.7058
90%	1.1038	0.6791
100%	1.1172	0.6625
110%	1.1288	0.6433
% of e	CF	ϕ_{3D}
95%	1.1297	0.6449
100%	1.1172	0.6626
110%	1.0924	0.6897
120%	1.0716	0.7088

Table 3: Variation in constriction factor and porosity depending on the variation in the diameter of the D_{hx} or thickness e in the wire screen $N_{WS} = 17$.

are dependent on the thickness as well, which seem to damp the effect of $1/e^2$. Nevertheless, one has to be cautious to generalise this to any geometry, and we cannot guarantee this trend when increasing the thickness of a screen.

Finally, another relevant aspect to highlight is that the use of a linear approximation as suggested by Wang et al. [66] is far from being accurate in asymmetric screens. Figures 10 and 11 show that the A_p/A_t curves do not have a linear trend at all and the derivative approaching $z = 0$ should be zero to ensure symmetry. The semi-analytical calculation introduced in the present work is a practical and realistic approach, which guarantees an accurate calculation of pore-related quantities.

4. Conclusions

In this work, a semi-analytical approach based on a discretisation procedure is proposed and applied to obtain relevant pore-related structural properties of interest for the ~~aerodynamic~~ characterisation of woven screens from easily measurable geometric parameters. This is the first work of its kind in the literature to create a ~~generalisable~~ generalised analytical model for the three-dimensional pore of symmetric/asymmetric screens.

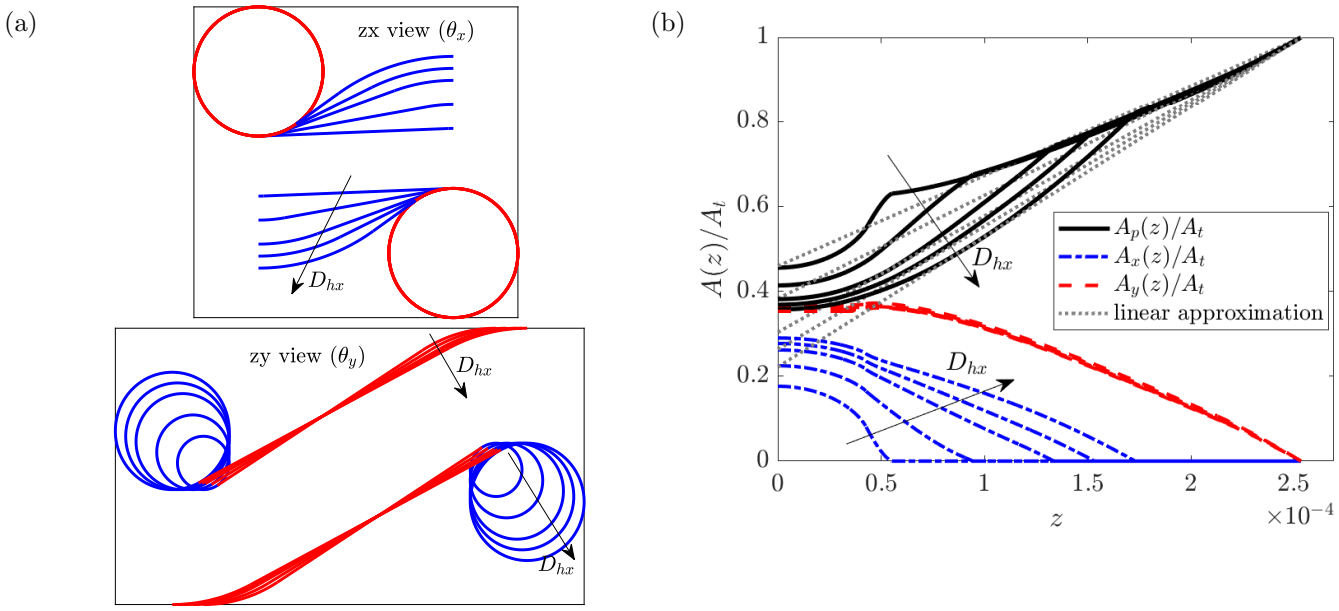

Figure 10: Effect of increasing the diameter D_{hx} with the OAT method on a) the wire screen geometry, and b) the local area of the pore A_p/A_t and area occupied by each thread (A_x for x-thread and A_y for y-thread) when intersected by the plane. Arrows indicate the trend of the plots when the parameter D_{hx} is increased. All units are in meters.

The Discretisation Method based on the different regions or stretches of the mesh pore is tested and validated. The results from its application show that the Discretisation Method outperforms the only single previous attempt in the literature which was not generalisable and assumed linearity. As expected, the study developed with the one-factor-at-a-time method illustrated several asymmetric mesh design which present abrupt changes in the evolution of the area of the pore along the thickness, for which a linear approximation underestimates notably the results. There are no analytical/semi-analytical works in the literature addressing this, thus to model (semi)analytically the mesh pores with high accuracy is an important contribution to estimate pore-related quantities such as e.g. the constriction factor, which is a structural parameter of the screen calculated by integration over the pore volume.

~~The Discretisation Method consists of an extendable approach to other types of screen by considering the different thread stretches that a perpendicular flow would cross through the screens, which is mimicked by the sweep of a plane parallel to the screen. This method takes into account the three-dimensional structure of the threads, which is often simplified in the literature to a two-dimensional shape in their aerodynamic characterisation. Thus, this semi-analytical approach~~

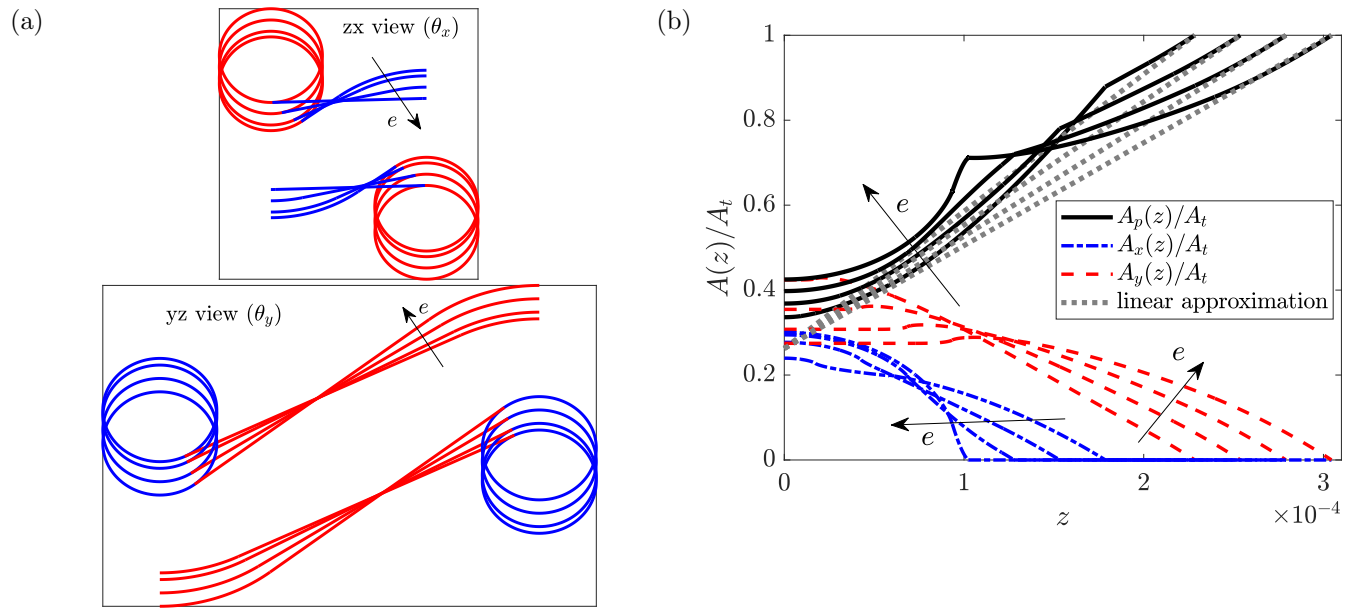

Figure 11: Effect of increasing the thickness of the screen e with the OAT method on a) the wire screen geometry, and b) the local area of the pore A_p/A_t and area occupied by each thread (A_x for x-thread and A_y for y-thread) when intersected by the plane. Arrows indicate the trend of the plots when the thickness is increased. All units are in meters.

~~is a valuable tool to calculate accurately certain pore-related parameters such as the constriction factor, which is a relevant quantity of interest in porous media but very poorly studied before in the literature. Actually, the constriction factor is a parameter usually ignored in the aerodynamic characterisation of screens, possibly because of the difficulty in its calculation.~~ Previous recent works suggested to model the evolution of the local area of the pore (from which the constriction factor and other pore-related parameters can be calculated) as a linear approximation, which has been demonstrated in the present investigation to be an imprecise estimation. Our proposed approach provides the only realistic and accurate calculation in the literature.

The semi-analytical model can be also used in design life cycles or optimisation algorithms in which the pore-related properties of new designs can be reliably estimated instantly for the first time. These values can be further input to e.g. existing permeability or ventilation models, as well as in computational simulations where these pore-related structural parameters are input as porous media boundary condition on screens represented by a thin surface. Therefore, the present approach is an important contribution also to decrease uncertainty in predictions that use these parameters as input. Wire/woven screens have plenty of applications in industry (insect-proof

screens in agriculture/buildings, heat transfer&mixing in chemical industry, mechanical screening, protection of turbines, electric safety switchgears, nanofluid wetting technology, textile design, control of turbulence, etc.), thus the impact of the present work is on many levels and disciplines.

~~The method has been tested and validated against a total of 20+4 wire screens from the literature, showing an outstanding accuracy. The applicability of this method to real screens provides additional support in the decision making and design of novel screens, as these are designed to maximise the fluid flow (e.g. ventilation in insect-proof screens for greenhouses) and minimise pressure drop and the pass of insects or objects. The current models for the characterisation of industrial screens are also based on simplified (usually bidimensional) parameters which large errors (especially those used in insect-proof screens for greenhouses) which could be improved with three-dimensional considerations. Therefore, our work may be the foundation for a more reliable characterisation that may enable new design paradigms in the field, as optimisation algorithms could be incorporated to deliver for the first time optimal *a la carte* woven screen designs that maximise e.g. ventilation (related to minimisation of the constriction factor, maximisation of porosity, etc.) and mechanical properties (e.g. more durable meshes with increased thickness but tight threads) under geometric optimisation constrains that block the pass of insects/objects of a specific size.~~ A limitation of the approach is the complexity in solving the integrals from the intersection between toroid and the plane, which have no solution in terms of elemental functions and thus must be solved by quadrature. This hinders the purely analytical definition of the method. A software to calculate relevant 3D pore-related parameters (AeroScreen) in the characterisation of screens is available as support to spread its application. Since the software admits manual input of data but also a text file from Euclides, an image detection software, all pore-related parameters can actually be estimated from pictures of the screens.

ACKNOWLEDGMENTS

The authors want to acknowledge the financial support from The Andalusian Research, Development and Innovation Plan (PAIDI—Junta de Andalucía) fundings and the research project UAL2020-AGR-A1916 within the FEDER-Andalucía 2014–2020 operational program.

Supplementary Material

The AeroScreen v1.0 code is available at
https://rsoftuma.uma.es/en/software/AeroScreen/.

References

[1] YS Cheng, HC Yeh, and KJ Brinsko. Use of wire screens as a fan model filter. Aerosol science and technology, 4(2):165–174, 1985.

[2] Alejandro Lopez-Martinez, Diego L. Valera Martínez, Francisco Molina-Aiz, Araceli Peña-Fernandez, and Patricia Marín-Membrive. Microclimate evaluation of a new design of insect-proof screens in a mediterranean greenhouse. Spanish Journal of Agricultural Research, 12(2):338, 2014.

[3] LX Nie, Y Yin, LY Yan, and SW Zhou. Pressure drop measurements and simulations for the protective mesh screen before the gas turbine compressor. In Proceedings of the 2nd International Conference on Green Energy, Environment and Sustainable Development (GEESD2021), pages 206–216. IOS Press, 2021.

[4] Lanre Oshinowo and David CS Kuhn. Turbulence decay behind expanded metal screens. The Canadian Journal of Chemical Engineering, 78(6):1032–1039, 2000.

[5] F Azizi and AM Al Taweel. Hydrodynamics of liquid flow through screens and screen-type static mixers. Chemical engineering communications, 198(5):726–742, 2011.

[6] John Kennedy, Eleonora Neri, and Gareth J Bennett. The reduction of main landing gear noise. In 22nd AIAA/CEAS Aeroacoustics Conference, page 2900, 2016.

[7] Zenong Cai, Xianhui Li, Xiaoling Gai, Bin Zhang, and Tuo Xing. An empirical model to predict sound absorption ability of woven fabrics. Applied Acoustics, 170:107483, 2020.

[8] A.F. Miguel and A.M. Silva. Porous materials to control climate behaviour of enclosures: an application to the study of screened greenhouses. Energy and Buildings, 31(3):195–209, 2000.

[9] TK Jayasree, BS Jinshah, V Lakshmi Visakha, and Tadepalli Srinivas. Assessment of air change effectiveness and thermal comfort in a naturally ventilated kitchen with insect-proof screen using CFD. Journal of Green Building, 16(3):37–56, 2021.

[10] Paraskevi Agrafioti, Sofia Faliagka, Evagelia Lampiri, Merle Orth, Mark Pätzel, Nikolaos Katsoulas, and Christos G Athanassiou. Evaluation of silica-coated insect proof nets for the control of aphis fabae, sitophilus oryzae, and tribolium confusum. Nanomaterials, 10(9):1658, 2020.

[11] RAJ Taylor, Sarit Shalhevet, Ishai Spharim, Menachem J Berlinger, and Sarah Lebiush-Mordechi. Economic evaluation of insect-proof screens for preventing tomato yellow leaf curl virus of tomatoes in Israel. Crop Protection, 20(7):561–569, 2001.

[12] Meir Teitel. The effect of screened openings on greenhouse microclimate. Agricultural and Forest Meteorology, 143(3-4):159–175, 2007.

[13] Alejandro López-Martínez, Francisco-Javier Granados-Ortiz, Francisco D Molina-Aiz, Choi-Hong Lai, María de los Ángeles Moreno-Teruel, and Diego L Valera-Martínez. Analysis of turbulent air flow characteristics due to the presence of a 13×30 threads·cm2 insect proof screen on the side windows of a mediterranean greenhouse. Agronomy, 12(3):586, 2022.

[14] Francisco-Javier Granados-Ortiz, Arrabal-Campos Francisco Manuel, and Alejandro et al. Lopez-Martinez. On the estimation of three-dimensional porosity of insect-proof screens. Computers and Electronics in Agriculture, 193:106639, 2022.

[15] Pranut Potiyaraj, Chutipak Subhakalin, Benchaphon Sawangharsub, and Werasak Udomkichdecha. Recognition and re-visualization of woven fabric structures. International Journal of Clothing Science and Technology, 22(2/3):79–87, 2010.

[16] Zuhaib Ahmad and Brigita Kolčavová Sirková. Analysis of mutual interlacing of threads in multifilament single layer and two layer woven fabric structure using Fourier series. The Journal of The Textile Institute, 111(1):93–107, 2019.

[17] Bilel Ben Boubaker, Bernard Haussy, and Jean-François Ganghoffer. Consideration of the yarn–yarn interactions in meso/macro discrete model of fabric: Part II: Woven fabric under uniaxial and biaxial extension. Mechanics Research Communications, 34(4):371–378, 2007.

[18] Caizheng Wang, Krishna Shankar, and Alan Fien. Finite element simulation of impact response of wire mesh screens. In EPJ Web of Conferences, volume 94, page 04033. EDP Sciences, 2015.

[19] Cameron Hall, Matthew Mason, Steven Psaltis, Matthew Chan, Eamon Conway, Brody Foy, Sayyed Mirnaziry, Danya Rose, Stephen Taylor, and Jakub Tomczyk. Structural modelling of deformable screens for large door openings. ANZIAM Journal, 57:M55–M114, 2015.

[20] M Assidi, B Ben Boubaker, and JF Ganghoffer. Equivalent properties of monolayer fabric from mesoscopic modelling strategies. International journal of solids and structures, 48(20):2920–2930, 2011.

[21] F Chaouachi, Y Rahali, and Jean-François Ganghoffer. A micromechanical model of woven structures accounting for yarn–yarn contact based on Hertz theory and energy minimization. Composites Part B: Engineering, 66:368–380, 2014.

[22] G Gopinath and RC Batra. Prediction of elastic moduli and ultimate strength of fiber/yarn-reinforced elastic–plastic matrix using Fourier series approach and cuboidal/wedge sub-volumes. International Journal of Non-Linear Mechanics, 125:103539, 2020.

[23] HA Aisyah, MT Paridah, SM Sapuan, RA Ilyas, A Khalina, NM Nurazzi, SH Lee, and CH Lee. A comprehensive review on advanced sustainable woven natural fibre polymer composites. Polymers, 13(3):471, 2021.

[24] Mahmood Ansar, Wang Xinwei, and Zhou Chouwei. Modeling strategies of 3D woven composites: A review. Composite structures, 93(8):1947–1963, 2011.

[25] DG Venkateshan, MM Amrei, AA Hemeda, Z Cullingsworth, J Corbett, and H Vahedi Tafreshi. Failure pressures and drag reduction benefits of superhydrophobic wire screens. Colloids and Surfaces A: Physicochemical and Engineering Aspects, 511:247–254, 2016.

[26] Anthony MJ Davis and Eric Lauga. The friction of a mesh-like super-hydrophobic surface. Physics of Fluids, 21(11):015103, 2009.

[27] Yongwei Cai, Shuo Li, Zhiliang Cheng, Guiying Xu, Xuejun Quan, and Yuting Zhou. Facile fabrication of super-hydrophobic fas modified electroless ni-p coating meshes for rapid water-oil separation. Colloids and Surfaces A: Physicochemical and Engineering Aspects, 540:224–232, 2018.

[28] Zenghui Zhao, Yoav Peles, and Michael K Jensen. Properties of plain weave metallic wire mesh screens. International Journal of Heat and Mass Transfer, 57(2):690–697, 2013.

[29] Marzena Iwaniszyn, Katarzyna Sindera, Anna Gancarczyk, Mateusz Korpyś, Roman J Jedrzejczyk, Andrzej Kołodziej, and Przemysław J Jodłowski. Experimental and CFD investigation of heat transfer and flow resistance in woven wire gauzes. Chemical Engineering and Processing-Process Intensification, 163:108364, 2021.

[30] Lawinska Katarzyna, Modrzewski Remigiusz, and Wodzinski Piotr. Mathematical and empirical description of screen blocking. Granular Matter, 18(1):1–10, 2016.

[31] AJ Álvarez, RM Oliva, A Jiménez-Vargas, and M Villegas-Vallecillos. A three-dimensional approach to the porous surface of screens. The Journal of The Textile Institute, 110(5):639–646, 2019.

[32] Antonio J Álvarez and Rocío M Oliva. Textile physical barriers against the Chestnut Gall Wasp *Dryocosmus kuriphilus*. Agronomy, 12(7):1728, 2022.

[33] Enrica Santolini, Beatrice Pulvirenti, Stefano Benni, Luca Barbaresi, Daniele Torreggiani, and Patrizia Tassinari. Numerical study of wind-driven natural ventilation in a greenhouse with screens. Computers and Electronics in Agriculture, 149:41–53, 2018.

[34] Meir Teitel, Shay Ozer, and Vered Mendelovich. Airflow temperature and humidity patterns in a screenhouse with a flat insect-proof screen roof and impermeable sloping walls–computational fluid dynamics (CFD) results. Biosystems Engineering, 214:165–176, 2022.

[35] Audberto Reyes-Rosas, Francisco D Molina-Aiz, Diego L Valera, Alejandro López, and Sasirot Khamkure. Development of a single energy balance model for prediction of temperatures inside a naturally ventilated greenhouse with polypropylene soil mulch. Computers and Electronics in Agriculture, 142:9–28, 2017.

[36] FD Molina-Aiz, DL Valera, and A López. Numerical and experimental study of heat and mass transfers in an Almería-type greenhouse. Acta Horticuturae, 1170:209–2018, 2017.

[37] B.J Bailey, J.I Montero, J.Pérez Parra, A.P Robertson, E Baeza, and R Kamaruddin. Airflow resistance of greenhouse ventilators with and without insect screens. Biosystems Engineering, 86(2):217–229, 2003.

[38] Alejandro López, Diego Luis Valera, Francisco Domingo Molina-Aiz, Francisco Javier Lozano, and Carlos Asensio. Sonic anemometry and sediment traps to evaluate the effectiveness of windbreaks in preventing wind erosion. Scientia Agricola, 74:425–435, 2017.

[39] Alejandro López-Martínez, Francisco Molina-Aiz, Diego Valera, and Karlos Espinoza-Ramos. Models for characterising the aerodynamics of insect-proof screens from their geometric parameters. Biosystems Engineering, 192:42–55, 2020.

[40] Ye Wang, Yilin Lin, Guang Yang, and Jingyi Wu. Flow physics of wicking into woven screens with hybrid micro-/nanoporous structures. Langmuir, 37(7):2289–2297, 2021.

[41] WN Septiadi, Nandy Putra, M Juarsa, IPA Putra, and R Sahmura. Characteristics of screen mesh wick heat pipe with nano-fluid as passive cooling system. Atom Indonesia, 39(1):24–31, 2013.

[42] Bruno Eckert and F Pfluger. The resistance coefficient of commercial round wire grids. Technical report, 1942. National Advisory Committee of Aeronautics.

[43] KEG Wieghardt. On the resistance of screens. Aeronautical Quarterly, 4(2):186–192, 1953.

[44] WT Wu, JF Liu, WJ Li, and WH Hsieh. Measurement and correlation of hydraulic resistance of flow through woven metal screens. International Journal of Heat and Mass Transfer, 48(14):3008–3017, 2005.

[45] Alejandro López, Francisco D Molina-Aiz, Diego L Valera, and Araceli Peña. Wind tunnel analysis of the airflow through insect-proof screens and comparison of their effect when installed in a mediterranean greenhouse. Sensors, 16(5):690, 2016.

[46] Chase Camarotti, Oscar Deng, Samuel Darr, Jason Hartwig, and JN Chung. Room temperature bubble point, flow-through screen, and wicking experiments for screen channel liquid acquisition devices. Applied Thermal Engineering, 149:1170–1185, 2019.

[47] Meir Teitel. Using computational fluid dynamics simulations to determine pressure drops on woven screens. Biosystems engineering, 105(2):172–179, 2010.

[48] W Abou-Hweij and F Azizi. CFD simulation of wall-bounded laminar flow through screens. Part I: Hydrodynamic characterization. European Journal of Mechanics-B/Fluids, 84:207–232, 2020.

[49] Luigi Formisano, Antonio Pannico, Christophe El-Nakhel, Giuseppe Starace, Milena Poledica, Stefania De Pascale, and Youssef Rouphael. Improved porosity of insect proof screens enhances quality aspects of zucchini squash without compromising the yield. Plants, 9(10):1264, 2020.

[50] F.D. Molina-Aiz, D.L. Valera, A.A. Peña, J.A. Gil, and A. López. A study of natural ventilation in an almería-type greenhouse with insect screens by means of tri-sonic anemometry. Biosystems Engineering, 104(2):224–242, 2009.

[51] Alejandro López-Martínez, Francisco D Molina-Aiz, Diego L Valera-Martínez, Javier López-Martínez, Araceli Peña-Fernández, and Karlos E Espinoza-Ramos. Application of semi-empirical ventilation models in a mediterranean greenhouse with opposing thermal and wind effects. use of non-constant cd (pressure drop coefficient through the vents) and cw (wind effect coefficient). Agronomy, 9(11):736, 2019.

[52] Donald A Nield, Adrian Bejan, et al. Convection in porous media, volume 3. Springer, 2006.

[53] James C Armour and Joseph N Cannon. Fluid flow through woven screens. AIChE Journal, 14(3):415–420, 1968.

[54] Meir Teitel. On the applicability of the Forchheimer equation in simulating flow through woven screens. Biosystems engineering, 109(2):130–139, 2011.

[55] Yangpeng Liu, Guoqiang Xu, Xiang Luo, Haiwang Li, and Jiandong Ma. An experimental investigation on fluid flow and heat transfer characteristics of sintered woven wire mesh structures. Applied Thermal Engineering, 80:118–126, 2015.

[56] W Bussière, D Rochette, Stéphane Clain, P André, and Jean-Baptiste Renard. Pressure drop measurements for woven metal mesh screens used in electrical safety switchgears. International Journal of Heat and Fluid Flow, 65:60–72, 2017.

[57] C Pérez Vega, JA Ramírez Arias, IL López Cruz, et al. Aerodynamic characteristics of anti-insect mesh windows used in greenhouses in mexico. Revista Mexicana de Ciencias Agrícolas, 7(3):493–506, 2016.

[58] Alejandro López Martínez, Francisco Domingo Molina Aiz, Diego Luis Valera Martínez, Ana Araceli Peña Fernández, and Karlos Espinoza. Effect of material ageing and dirt on the

behaviour of greenhouse insect-proof screens. Spanish journal of agricultural research, 16(4):4, 2018.

[59] Fouad Azizi. On the pressure drop of fluids through woven screen meshes. Chemical engineering science, 207:464–478, 2019.

[60] Carl Fredrik Berg. Permeability description by characteristic length, tortuosity, constriction and porosity. Transport in porous media, 103(3):381–400, 2014.

[61] Carl Fredrik Berg. Re-examining Archie's law: conductance description by tortuosity and constriction. Physical Review E, 86(4):046314, 2012.

[62] Francis AL Dullien. Porous media: fluid transport and pore structure. Academic press, 2012.

[63] JÜRGEN R SCHOPPER. A theoretical investigation on the formation factor/permeability/porosity relationship using a network model. Geophysical prospecting, 14(3):301–341, 1966.

[64] LM Schwartz, N Martys, DP Bentz, EJ Garboczi, and S Torquato. Cross-property relations and permeability estimation in model porous media. Physical Review E, 48(6):4584, 1993.

[65] Jacob Bear. Dynamics of fluids in porous media. Dover Publications. INC, New York, 1988.

[66] Ye Wang, Guang Yang, Yiye Huang, Yonghua Huang, Rui Zhuan, and Jingyi Wu. Analytical model of flow-through-screen pressure drop for metal wire screens considering the effects of pore structures. Chemical Engineering Science, 229:116037, 2021.

[67] AJ Álvarez, RM Oliva, and DL Valera. Software for the geometric characterisation of insect-proof screens. Computers and electronics in agriculture, 82:134–144, 2012.

[68] Frederick Thomas Peirce. 5—the geometry of cloth structure. Journal of the Textile Institute Transactions, 28(3):T45–T96, 1937.

[69] BK Behera, Pramod Kumar Hari, and Ahmad Rashed Labanieh. Modelling the structure of woven fabrics. In Woven Textiles, pages 291–328. Elsevier, 2020.

[70] Granados-Ortiz, F.-J., and Lopez-Martinez, A., and Arrabal-Campos F. M. Poro3D v1.0. https://rsoftuma.uma.es/en/software/poro3d/, Accessed: 2021-12-13.

[71] EC Cady. Study of thermodynamic vent and screen baffle integration for orbital storage and transfer of liquid hydrogen. Technical report, 1973.

[72] Norfarina Muhamad Nor, Mohd Shamzi Mohamed, Teck Chwen Loh, Hooi Ling Foo, Raha Abdul Rahim, Joo Shun Tan, and Rosfarizan Mohamad. Comparative analyses on medium optimization using one-factor-at-a-time, response surface methodology, and artificial neural network for lysine–methionine biosynthesis by Pediococcus pentosaceus RF-1. Biotechnology & Biotechnological Equipment, 31(5):935–947, 2017.

Appendix A. Appendix: Intersection between a plane and a toroid and cylinder.

Appendix A.1. Intersection between torus and plane

In a general form, the parametric equations that model a torus generated by rotation around the x-axis and centered in $(0, 0, 0)$ take the form:

$$\begin{aligned} x(u, v) &= R_2 \sin(v), \\ y(u, v) &= (R_1 + R_2 \cos(v)) \cos(u), \\ z(u, v) &= (R_1 + R_2 \cos(v)) \sin(u), \end{aligned} \tag{A.1}$$

with R_1 the radius of the rotation around the x-axis, R_2 the radius of the circumference in rotation of centre positioned at R_1 distance to the centre of coordinates, $u \in [0, 2\pi]$ the angle that R_1 sweeps, and $v \in [0, 2\pi]$ the angle that R_2 sweeps. When a halved torus ($z(u, v) \geq 0$) is cut by a plane orthogonal to the toroid, i.e. $z(x,\ y) = z' = constant$, depending on the height z', one can obtain three different cross-sections (spiric sections of a torus): one oval or ellipse cross-section (if $z' > R_1 - R2$) [hereinafter named Type 1 cross-section], a lemniscate-like cross-section (if $z' = R_1 - R_2$) [hereinafter named Type 2 cross-section], or two ovals (if $z' < R_1 - R_2$) [hereinafter named Type 3 cross-section], see Figure A.12. For each of these cases, the parametric equations of the cross-section curves are the same, which can be obtained by equality in z:

$$\begin{aligned} x(v) &= R_2 \sin(v), \\ y(v) &= (R_1 + R_2 \cos(v)) \sqrt{1 - \left(\frac{z'}{R_1 + R_2 \cos(v)} \right)^2}, \end{aligned} \tag{A.2}$$

with $v \in [0, 2\pi]$. Although these equations are valid for the three types of cross-section, the limits of v must be carefully chosen. Must be pointed out that, when $\left(\frac{z'}{R_1 + R_2 \cos(v)} \right)^2 > 1$, then complex numbers appear. Although they make no contribution to the parametric curve, they can be avoided by simply selecting v as:

$$\cos^{-1}\left(-\frac{z' - R_1}{R_2} \right) \leq v \leq \cos^{-1}\left(\frac{z' - R_1}{R_2} \right). \tag{A.3}$$

Thus, this also states the values of the limits in the integration to estimate the area of the cross-section for each type of cut. The area enclosed by the parametric curve in the yx plane can be obtained by the integral:

$$A_{tor}(z) = \int_1^2 x(y) dy = \int_{v_1}^{v_2} x(v) \frac{dy(v)}{dv} dv = \int_{v_1}^{v_2} (R_2 \sin(v)) \left(\frac{-R_2 \sin(v)}{\sqrt{1 - \left(\frac{z}{R_1 + R_2 \cos(v)} \right)^2}} \right) dv, \tag{A.4}$$

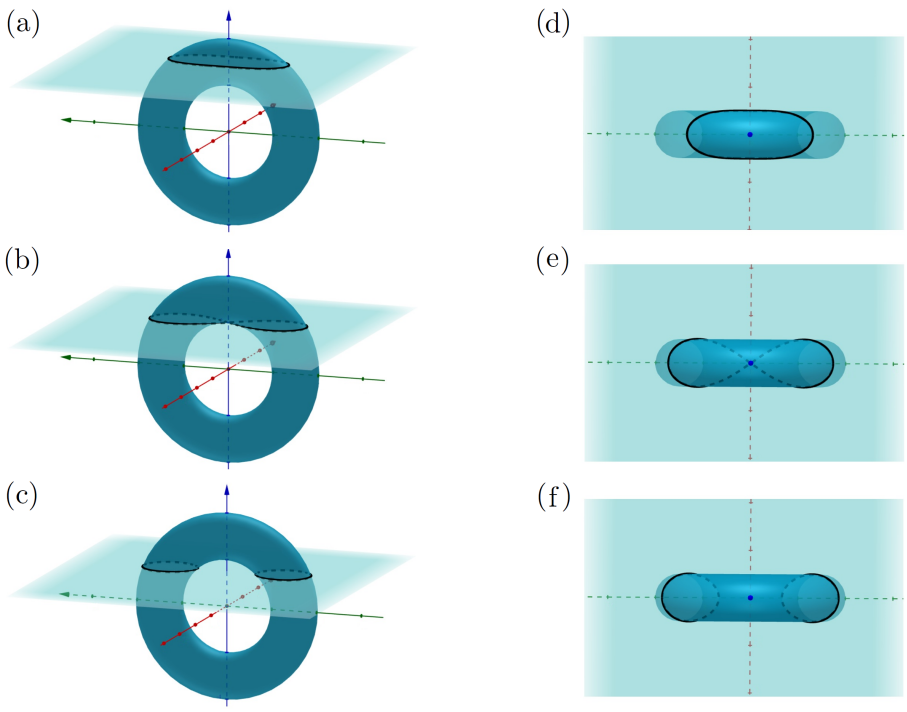

Figure A.12: Different cross-sections of a torus generated by revolution around the x-axis. The left column illustrates the isometric views of the a) Type 1 cross-section, b) Type 2 cross-section, and c) Type 3 cross-section; whereas the right column of plots illustrates the top views of the d) Type 1 cross-section, e) Type 2 cross-section, and f) Type 3 cross-section.

where v_1 and v_2 are the limits of the integral such that $v \in [v_1, v_2]$. These limits, taking into account (A.3) and the limiting state $z' = R_1 - R_2$, are as follows:

$$\begin{gathered}\cos^{-1}\left(-\tfrac{z'-R_1}{R_2}\right) \leq v \leq \cos^{-1}\left(\tfrac{z'-R_1}{R_2}\right), \text{if cross-section is of Type 1 or 2 } (z' \geq R_1 - R_2), \\ -\pi \leq v \leq \pi, \text{if cross-section is of Type 3 } (z' < R_1 - R_2).\end{gathered} \tag{A.5}$$

The greatest problem in the calculation of the area of the cross-section arises from the fact that the integral in Equation (A.4) has no solution in term of elemental functions. This type of integral is very complex, not even solvable by means of either approximations or series. To our knowledge, the only promising mathematical approach might be related to the use of elliptic integration, as done in other similar curves such as Cassini ovals, which are often incorrectly referred to as spiric toric sections. However, as these potential solutions to the integral need to be further integrated (to estimate the constriction factor, the area will be integrated along the thickness of the screen), this would complicate the problem excessively, and a solution with elemental functions to the analytical equations does not exist. Therefore, although the present paper provides analytical

integral equations to model the evolution of pore, the integrals of the toroid cross-sections have to be solved inevitably by quadrature.

Appendix A.2. Intersection between cylinder and plane

The parametric equations of an inclined cylinder volume are:

$$\begin{aligned} x(l,\, s) &= l\cos\theta + R\sin s\sin\theta, \\ y(l,\, s) &= R\cos s, \text{ with } l \in [-l_{cyl}/2,\, l_{cyl}/2] \text{ and } s \in [0,\, 2\pi), \\ z(l,\, s) &= R\sin s\cos\theta - l\sin\theta, \end{aligned} \tag{A.6}$$

where l_{cyl} is the length of the cylinder, R is the radius and θ the angle of inclination. The intersection between the plane $z = z'$ and the cylinder allows to obtain its cross-section. The parametric equations of such cross-section are obtained from equality in z:

$$\begin{aligned} x(s) &= R\cos(s), \\ y(s) &= \frac{z' - R\sin(s)\cos(\theta)}{\sin(\theta)}\cos(\theta) - R\sin(s)\sin(\theta), \end{aligned} \tag{A.7}$$

where $s \in [0, 2\pi]$.

Similarly to the analysis for the toroid, the area integral of the cross-section of the cylinder can be obtained as:

$$\begin{gathered} A_{cyl}(z) = \int_{s_1}^{s_2} x(s)\frac{dy(s)}{ds}ds = \\ \int_{s_1}^{s_2} \left(R_{hy}\cos(s)\right)\left(\frac{R_{hy}\cos(s)}{\sin(\theta_y)}\right)ds = \frac{R_{hy}^2}{\sin(\theta_y)}\left[\tfrac{1}{2}(s + \sin(s)\cos(s)\right]_{s_1}^{s_2}, \end{gathered} \tag{A.8}$$

where $s \in [s_1,\, s_2] = [0, 2\pi]$ if the full area is desired. However, as the cylinder will be joined to pieces of toroid portions to form a thread geometry, the area will be constrained, thus s_1 and s_2 limits will have dependence with z'. This is discussed in Section 2.3.

Appendix B. Application of the approach via stretches for the calculation of the volume integral of the pore with separation of integrals.

For the calculation of the constriction factor the area of the pore is integrated in two different ways: with respect to z (volume of the pore, V_p), and also the inverse of the area with respect to z. Since the area of the pore varies with z, it can be modelled as $A_p(z) = A_t - (A_x(z) + A_y(z))$, with $A_x(z)$ and $A_y(z)$ the area of the intersection of the plane parallel to the screen at z and the

x-thread and y-thread, respectively. Thus, when A_p is integrated, this integral can be decomposed into:

$$V_p = 2\int_0^{e/2} \left(A_t - (A_x(z) + A_y(z))\right) dz = 2\int_0^{e/2} A_t dz - 2\left(\int_0^{e/2} A_x(z)dz + \int_0^{e/2} A_y(z)dz\right). \quad \text{(B.1)}$$

This decomposition of the integral allows to work on each term separately, not requiring to solve a larger complex multivariate integral (must be recalled that $A_x(z)$ and $A_y(z)$ are actually integrals). Unfortunately, this is not possible for the integration of $1/A_p(z)$, as will be shown in the next subsection of the appendix.

By taking into account the different stretches mentioned in Section 2.3, one should perform the calculation carefully for the x- and y-threads separately and by adding/removing any stretch depending on the geometry. The AeroScreen software performs this identification&assignation automatically in advance.

When intersected at different z values, the sweeping will include as maximum the six stretches described in Section 2.3 (actually, it is expected to include from two to four for each thread). The volume occupied by the i-thread (thus j-thread stands for the other thread) at each Stretch k will be denoted by V_{ki}, which will be lately subtracted to the total volume of the pore. Thus, the volume integrals, limited by the stretches $\mathcal{S}_k$ in z and by the limiting angles v_{lim} for the pieces of torus, and by s_{lim} for the cylinders, are:

$$V_{1i} = 2\int_{S_1} A_{1i}(z)dz = 2\int_{zp_1^i}^{zp_0^i} \int_0^{v_{lim1}^i(z)} \frac{R_{hi}^2 \sin(v)^2}{\sqrt{1 - \left(\frac{z-O_{iz}}{a+R_{hi}\cos(v)}\right)^2}} dv dz, \quad \text{(B.2)}$$

$$V_{2i} = 2\int_{S_2} A_{2i}(z)dz =$$
$$2\left(\int_{zp_2^i}^{zp_1^i} \int_{v_{lim2}^i(z)}^{v_{lim1}^i(z)} \frac{R_{hi}^2 \sin(v)^2}{\sqrt{1-\left(\frac{z-O_{iz}}{a+R_{hi}\cos(v)}\right)^2}} dv dz + \int_{zp_2^i}^{zp_1^i} \frac{2R_{hi}^2}{\sin(\theta_i)} \left[\frac{1}{2}(s + \sin(s)\cos(s)\right]_{s=s_{lim}^i(z)}^{s=\pi/2} dz\right), \quad \text{(B.3)}$$

$$V_{3i} = 2\int_{S_3} A_{3i}(z)dz =$$
$$2\left(\int_{zp_3^i}^{zp_2^i} \int_{v_{lim3}^i(z)}^{v_{lim2}^i(z)} \frac{R_{hi}^2 \sin(v)^2}{\sqrt{1-\left(\frac{z-O_{iz}}{a+R_{hi}\cos(v)}\right)^2}} dv dz + \int_{zp_3^i}^{zp_2^i} \frac{2R_{hi}^2}{\sin(\theta_i)} \left[\frac{1}{2}(s + \sin(s)\cos(s)\right]_{s=s_{lim}^i(z)}^{s=\pi/2} dz\right), \quad \text{(B.4)}$$

$$V_{4i} = 2\int_{S_4} A_{4i}(z)dz = 2\int_{zp_4^i}^{zp_3^i} \frac{4R_{hi}^2}{\sin(\theta_i)} \left[\frac{1}{2}(s + \sin(s)\cos(s)\right]_{s=0}^{s=\pi/2} dz, \quad \text{(B.5)}$$

$$V_{5i} = 2\int_{S_5} A_{5i}(z)dz =$$

$$2\left(\int_{zp_5^i}^{zp_4^i}\int_{v_{lim3}^i(z)}^{v_{lim2}^i(z)} \frac{R_{hi}^2\sin(v)^2}{\sqrt{1-\left(\frac{z-O_{iz}}{a+R_{hi}\cos(v)}\right)^2}}dvdz + \int_{zp_5^i}^{zp_4^i}\frac{2R_{hi}^2}{\sin(\theta_i)}\left[\frac{1}{2}(s+\sin(s)\cos(s)\right]_{s=s_{lim}^i(z)}^{s=s_{lim2}^i(z)}dz \quad + \right.$$
$$\left. \int_{zp_5^i}^{zp_4^i}\int_{v'^i_{lim2}(z)}^{\pi} \frac{R_{hi}^2\sin(v)^2}{\sqrt{1-\left(\frac{z+O_{iz}}{a+R_{hi}\cos(v)}\right)^2}}dvdz\right) \tag{B.6}$$

$$V_{6i} = 2\int_{S_6} A_{6i}(z)dz =$$

$$2\left(\int_{0}^{zp_5^i}\int_{v_{lim3}^i(z)}^{v_{lim2}^i(z)} \frac{R_{hi}^2\sin(v)^2}{\sqrt{1-\left(\frac{z-O_{iz}}{a+R_{hi}\cos(v)}\right)^2}}dvdz + \int_{0}^{zp_5^i}\frac{2R_{hi}^2}{\sin(\theta_i)}\left[\frac{1}{2}(s+\sin(s)\cos(s)\right]_{s=s_{lim}^i(z)}^{s=s_{lim2}^i(z)}dz \quad + \right.$$
$$\left. \int_{0}^{zp_5^i}\int_{v'^i_{lim2}(z)}^{v'^i_{lim1}(z)} \frac{R_{hi}^2\sin(v)^2}{\sqrt{1-\left(\frac{z+O_{iz}}{a+R_{hi}\cos(v)}\right)^2}}dvdz\right) \tag{B.7}$$

with

$$zp_0^j = R_{hj} + \frac{h_j}{2} \text{ and } zp_0^i = e/2 \text{ (for } \textit{configuration 1} \text{ and } i = x), \tag{B.8}$$

$$zp_0^i = R_{hi} + \frac{h_i}{2} \text{ and } zp_0^j = e/2 \text{ (for } \textit{configuration 2} \text{ and } i = x), \tag{B.9}$$

$$zp_1^i = (R_{hj} + D_{hi})\cos(\theta_i) - \frac{h_j}{2}, \tag{B.10}$$

$$zp_2^i = R_{hj} - \frac{h_j}{2}, \tag{B.11}$$

$$zp_3^i = R_{hj}\cos(\theta_i) - \frac{h_j}{2}, \tag{B.12}$$

$$zp_4^i = \frac{h_j}{2} - R_{hj}\cos(\theta_i), \tag{B.13}$$

$$zp_5^i = \frac{h_j}{2} - R_{hj}. \tag{B.14}$$

It must be noted that if any of these limits is negative, the value of the limit in the integral must set to zero (we are integrating between 0 and $e/2$) and the stretch must be selected carefully. For instance, attention must be paid to not overlap $\mathcal{S}_2$ with $\mathcal{S}_5$ or $\mathcal{S}_6$, as their ranges may actually overlap in many WSs. This is solved by rearranging the limits according to their intersection. Finally the volume of the pore can be calculated as:

$$V_p = 2\int_0^{e/2} A_t dz - 2\left(\sum_{k=1}^{N_{Si}} V_{ki} + \sum_{k=1}^{N_{Sj}} V_{kj}\right), \tag{B.15}$$

where A_t is the total area $A_t = (L_{px}+D_{hy})(L_{py}+D_{hx})$, and N_{Si} and N_{Sj} are the number of stretches in the intersection between the plane parallel to the screen and the i and j-thread, respectively.